nature geoscience

Article

https://doi.org/10.1038/s41561-026-01922-5

Urban black-carbon radiative heating intensified by biogenic–anthropogenic interactions

Received: 14 July 2025

Accepted: 9 January 2026

A list of authors and their affiliations appears at the end of the paper

Black carbon is a global climate forcer due to its strong radiative absorption, which is highly sensitive to coating formation regulated by anthropogenic and biogenic emissions. However, how cross-regional biogenic sources modulate urban black carbon coating and radiative effects remains poorly understood. Here we integrate observations and model simulations to investigate such biogenic–anthropogenic interactions in eastern China. The results show that biogenic volatile organic compounds from vegetation-rich regions undergo atmospheric oxidation to produce oxygenated organic compounds, which are subsequently advected into downwind urban areas. These products enhance regional atmospheric oxidation capacity and supply additional precursors, thereby promoting secondary organic aerosol production. This biogenic-induced strengthening of regional photochemistry drives the formation of highly oxidized secondary organic aerosol coatings on black carbon and increases its fraction within the total particle population. Consequently, black carbon absorption efficiency increases more steeply with the coating carbon oxidation state under biogenic-rich conditions, yielding an average ~20% enhancement in radiative absorption from the lensing effect relative to biogenic-poor periods. Our findings reveal that cross-regional biogenic–anthropogenic interactions enhance both the formation and particle population fraction of secondary organic aerosol coatings on urban black carbon, potentially further amplifying its radiative effects as biogenic emissions increase under future warming scenarios.

Black carbon (BC) is a global short-lived climate forcer that exerts warming effects by strongly absorbing solar radiation[1–3]. Once emitted, primarily through incomplete combustion of fossil fuels and biomass, BC undergoes atmospheric ageing, transitioning from externally mixed to internally mixed states as it acquires coatings of secondary organic and inorganic matter[4–8]. These coatings act as optical lenses that amplify its radiative absorption by up to several fold[9,10]. Consequently, understanding the environmental factors that modulate BC ageing and its associated radiative effects is essential for constraining its climate impacts[6,11,12].

Chemical transformation and optical properties of BC are strongly influenced by the surrounding atmospheric composition[6,8,13–15]. In mid-latitude regions where densely vegetated landscapes adjoin megacity corridors[16], such as eastern USA[17], western Europe[18], South America[19] and eastern Asia[20], biogenic volatile organic compounds (BVOCs) frequently mix with anthropogenic pollutants, shaping critical atmospheric chemical processes[21,22] and modulating the atmospheric composition over downwind urban areas[18,23]. Eastern China offers a particularly representative and globally relevant example[23,24]. During summer, prevailing meteorological patterns—driven by

e-mail: jingyili@nuist.edu.cn; xinlei@seu.edu.cn

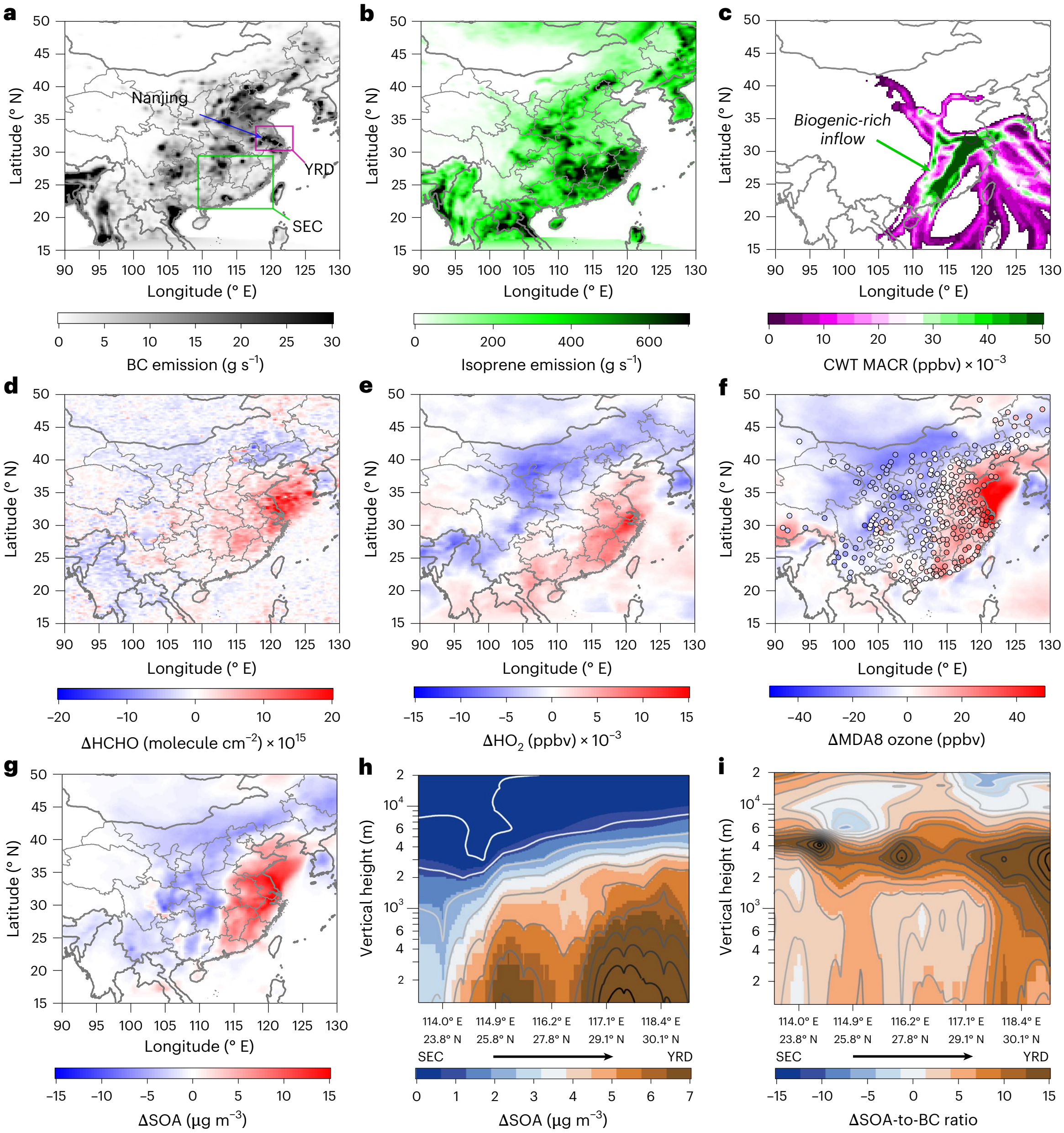

Fig. 1 | Biogenic transport enhances atmospheric oxidation and secondary production. a,**b**, Spatial distributions of anthropogenic (BC) and biogenic (isoprene) emissions during the entire field observation period. **c**, Geographical origins of MACR from concentration-weighted trajectory analysis. **d**, TROPOMI-retrieved HCHO column differences between biogenic-rich and biogenic-poor periods. **e**, Modelled differences in HO_2 radicals. **f**, Observed and simulated differences in MDA8 ozone. **g**, Modelled differences in SOA concentrations. **h**, Modelled SOA differences along the transport pathway from southeastern China (SEC, left) to the Yangtze River Delta (YRD, right). **i**, Modelled SOA-to-BC mass ratio differences along the SEC–YRD transport pathway.

the East Asian summer monsoon[25] and subtropical high-pressure systems[26,27]—frequently facilitate large-scale transport of air masses from vegetation-rich southeast China towards the densely populated and heavily polluted urban clusters in the north[23,27]. However, the extent to which such cross-regional biogenic–anthropogenic interactions modify BC ageing and radiative properties in downwind urban areas remains unclear. The underlying mechanisms and climate-forcing implications warrant systematic evaluations.

Here we address this gap by integrating ground-based observations, satellite retrievals and regional chemical transport modelling to investigate the coupled chemical and radiative effects of biogenic–anthropogenic interactions in eastern China. We identify that BVOC oxidation products from southeast China are regularly transported to the downwind urban regions, resulting in enhanced atmospheric oxidation capacity, BC ageing and subsequent atmosphere radiative heating. This study reveals a previously underappreciated mechanism through which large-scale biogenic–anthropogenic interactions intensify BC climate-relevant effects, offering critical insights into the multiscale coupling between biogenic and anthropogenic emissions, atmospheric composition and regional climate forcing.

Cross-regional biogenic transport and oxidation products

BVOCs, such as isoprene, can be rapidly oxidized in the atmosphere, generating reactive intermediates including formaldehyde (HCHO), methacrolein (MACR) and some semi-volatile or intermediate-volatility organic compounds[28,29]. These oxygenated VOCs (OVOCs) can be transported over long distances and play a critical role in shaping regional

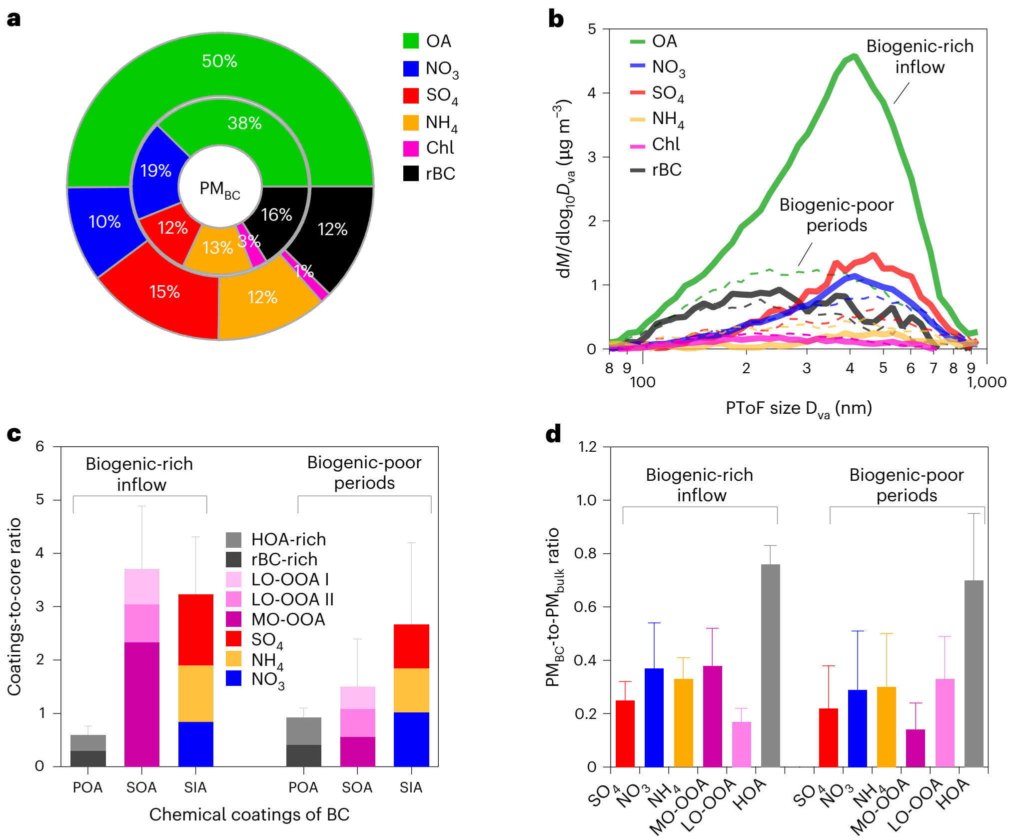

Fig. 2 | Chemical coatings of BC-containing particles. a, Relative chemical composition of coatings on BC-containing particles during biogenic-rich (outer ring) and biogenic-poor (inner ring) periods. **b**, Size-resolved mass distributions of BC-containing particles for biogenic-rich versus biogenic-poor periods. **c**, Ratios of total coating mass to BC core mass during biogenic-rich and biogenic-poor periods. Data represent mean ± standard deviation (s.d.) (calculated from $n = 120$ and $n = 315$ data points, respectively). **d**, Comparison between the chemical composition of coatings on BC-containing particles and the bulk PM$_{2.5}$ composition under biogenic-rich and biogenic-poor periods. Data represent mean ± s.d. (calculated from $n = 120$ and $n = 307$ data points, respectively).

atmospheric chemistry[23,30,31]. During a summertime field campaign in 2023 in urban Nanjing, located in the Yangtze River Delta (YRD) of eastern China, we observed representative inflows of BVOC oxidation products undergoing regional transport. On the basis of anthropogenic and biogenic emission analysis (Methods), we confirmed distinct spatial patterns during the observation period (Fig. 1a,b). Anthropogenic BC emissions were concentrated in central and northern China, whereas biogenic emissions dominated the south and southeast. Nanjing, situated on the western edge of the YRD region, lies within a hotspot of high BC emissions (Fig. 1a). MACR is a prominent oxidation product of isoprene (C_5H_8) under hydroxyl radical (OH) rich conditions. As shown in Fig. 1c, analysis combining the back-trajectory model with MACR measurements revealed transport pathways carrying elevated MACR from southeastern China (SEC) into the YRD region. Time series of MACR (Extended Data Fig. 2a,b), transport pathways (Fig. 1c) and backward air mass trajectories (Extended Data Fig. 1 and Supplementary Fig. 1) together defined two regimes: (1) biogenic-rich periods, characterized by sustained high MACR levels and transport across densely vegetated SEC (Fig. 1b) and (2) biogenic-poor periods, with low MACR levels and air masses largely bypassing vegetated regions. Satellite retrievals of HCHO columns from Tropospheric Monitoring Instrument (TROPOMI) (Fig. 1d) further support this classification, revealing marked enhancements (~1.1×10^{16} molecule cm^{-2}) in the SEC–YRD corridor during biogenic-rich inflows. These enhancements were reproduced by regional chemical transport simulations, which showed elevated surface HCHO (4–7 parts per billion by volume (ppbv); Extended Data Fig. 3a) and MACR (up to 1.2 ppbv; Extended Data Fig. 3b) along the same pathway. Concurrent increases in hydroperoxy radicals (HO_2) (~18 pptv; Fig. 1e), a key radical in tropospheric ozone formation[32], were also simulated across the YRD region. Sensitivity experiments with the chemical transport model (Extended Data Fig. 4 and Methods) confirmed that during biogenic-rich periods, HCHO and HO_2 levels over eastern China were strongly influenced by BVOC emissions from southeastern China, whereas anthropogenic VOCs had negligible effects.

Surface observations of maximum daily 8-h average (MDA8) ozone during biogenic products advection episodes displayed spatial patterns that mirrored those of OVOCs and HO_2, with model simulations in close agreement (Fig. 1f). Sensitivity analyses also further demonstrated that ozone levels were strongly affected by biogenic inflows, whereas anthropogenic VOCs had minimal effects from the SEC region (Extended Data Fig. 4). These results indicate that regional biogenic inflows substantially elevate atmospheric oxidation capacity and promote ozone formation in downwind urban clusters in the YRD region. To assess the climatological importance of such processes, we analysed summertime air mass trajectories (Supplementary Fig. 2) and ozone anomalies (Supplementary Fig. 3) over 2013–2023. Using trajectory-based classifications and MACR measurements analogous to that in Fig. 1c, we identified biogenic-rich inflows each year and quantified the associated ozone enhancements relative to biogenic-poor conditions. Biogenic-rich air masses occurred each summer, with frequencies ranging from 18% to 65% (Supplementary Fig. 2) and consistently yielded elevated ozone levels (approximately 10–60%) in the YRD region (Supplementary Fig. 3), confirming the recurring nature of this cross-regional mechanism. Beyond ozone enhancement, biogenic inflows also modulate the chemical sensitivity of ozone production. As shown in Extended Data Fig. 5, NO_x concentrations in the YRD

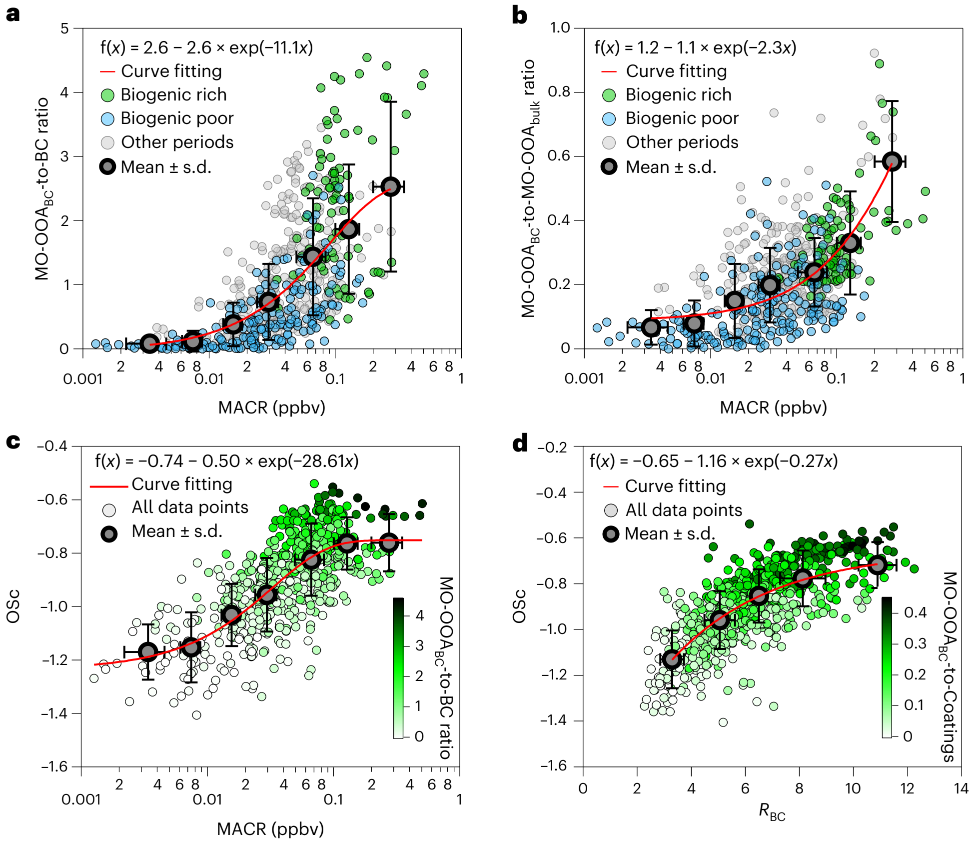

Fig. 3 | Secondary organic coating formation of BC particles. **a**, Mass ratio of MO-OOA coatings to BC core as a function of MACR. **b**, Ratio of MO-OOA$_{BC}$ in BC particle coatings to that in $PM_{2.5}$ bulk aerosol as a function of biogenic MACR concentrations, indicating preferential partitioning under enhanced biogenic influence. **c**, Relationship between the oxidation state (OSc) of BC coatings and MACR levels. **d**, Relationship between OSc and the coating-to-core mass ratio (R_{BC}) by mass. Error bars represent the s.d. of data points within each bin.

region remained relatively constant during both biogenic-rich and biogenic-poor periods. However, the chemical regime—diagnosed using the satellite-derived $HCHO/NO_2$ column ratio (Methods)—shifted from a VOC-limited regime towards NO_x-limited or transitional conditions under biogenic-rich inflows. This shift highlights the critical role of BVOCs in altering atmospheric oxidation chemistry and enhancing ozone production efficiency[23,33].

Chemical transport model simulations also revealed spatially coherent increases in secondary organic aerosol (SOA) concentrations, consistent with elevated ozone, OVOCs (for example, HCHO and MACR) and HO_2 levels (Fig. 1e–g and Extended Data Fig. 3), with SOA reaching up to ~17 μg m^{-3} in the YRD region. According to the transport pathway from trajectory-based analysis (Fig. 1c), we further extracted the vertical profiles of simulated SOA concentrations along the regional transport pathway. Figure 1h shows the SOA enhancement during biogenic-rich periods (relative to biogenic poor), with pronounced accumulation in the lower troposphere, peaking above 5 μg m^{-3} within around 1 km altitude. By contrast, changes in the SOA-to-BC ratio exhibited a distinct pattern, with maxima concentrated at higher altitudes (~4 km) and elevated values extending throughout the YRD column from near surface to the upper troposphere (Fig. 1i). To further isolate the role of biogenic emissions from the SEC region, we conducted a sensitivity simulation by turning off BVOC emissions in the SEC region (Supplementary Fig. 4). In contrast to the high surface SOA levels over the YRD region in the base case, disabling SEC biogenic emissions led to substantial SOA reductions along the transport pathway and through the vertical column (Supplementary Fig. 4a,b), underscoring the critical role of biogenic inflows in enhancing SOA in the YRD region.

To quantify the source contributions to SOA in the YRD region during biogenic-rich periods, we applied source apportionment using the chemical transport model (Extended Data Fig. 6 and Methods). Regionally transported SOA from the SEC region and local SOA from within the YRD contributed approximately 48% and 34% to surface SOA, respectively. Contributions from anthropogenic SOA (ASOA) and biogenic SOA (BSOA) were comparable: SEC-derived ASOA and BSOA accounted for ~26% and ~22%, whereas YRD-local ASOA and BSOA contributed ~15% and ~19%, respectively. For column-integrated SOA, SEC and YRD sources contributed ~52% and ~11%, respectively, with total column SOA consisting of ~56% ASOA and ~44% BSOA. Notably, ASOA from local emissions increased by ~12% during biogenic-rich periods, despite anthropogenic emissions remaining relatively stable. These modelling results are overall consistent with observational source apportionment from positive matrix factorization (PMF) analysis of organic spectra in non-refractory fine particulate matter (NR-$PM_{2.5}$) measured by a time-of-flight aerosol chemical speciation monitor (ToF-ACSM). During the entire campaign, the average organic aerosol (OA) concentrations were 5.9 μg m^{-3}, higher during biogenic-rich periods (9.7 μg m^{-3}) than biogenic-poor periods (4.1 μg m^{-3}) and about two-fold lower than summer values reported in urban Beijing (~12.6 μg m^{-3}) (ref. 34). In this study, the contribution of OA to $PM_{2.5}$ increased from ~47% during biogenic-poor periods to 61% during biogenic-rich periods, corresponding to a ~137% increase in organic-mass concentration (Supplementary Fig. 5). Moreover, the SOA factors associated with biogenic-rich conditions, namely low oxidized oxygenated organic aerosol (LO-OOA$_{bulk}$) and more oxidized oxygenated organic aerosol (MO-OOA$_{bulk}$) in $PM_{2.5}$, showed substantial increases, with total SOA concentrations rising by ~254% relative to biogenic-poor periods.

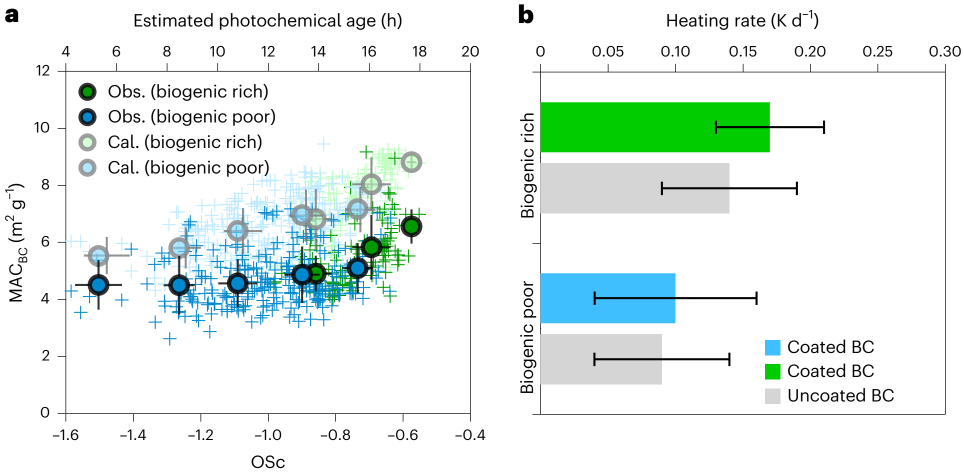

Fig. 4 | Radiative heating enhancement induced by BC. a, Relationship between the observed (obs.) and calculated (cal.) mass absorption cross section of BC at 880 nm (MAC_{BC}) and the oxidation state (OSc) of BC-containing particles. Both the biogenic-rich and biogenic-poor periods were processed using the same OSc bin intervals (ranging from −1.4 to −0.4 with a step of 0.2). For each bin, we selected the corresponding data points and calculated the mean values of MAC and OSc. Error bars represent the s.d. of data points within each bin. The estimated photochemical age was derived based on the relationship shown in Supplementary Fig. 6. **b**, Comparison of the estimated net radiative heating rate during periods dominated by biogenic-rich versus biogenic-poor conditions. Green and blue bars represent BC with secondary organic coatings under biogenic-rich and biogenic-poor conditions, respectively, whereas grey bars represent uncoated BC without coatings. Data represent mean ± s.d. (calculated from $n = 19$ (biogenic-rich) and $n = 37$ (biogenic-poor) data points, respectively).

Correspondingly, model simulations showed a ~196% increase in surface SOA across the YRD region. In particular, the MO-OOA_{bulk}—a representative-aged SOA factor typically linked to regional transport—increased by ~87% under biogenic-rich conditions compared to biogenic-poor periods. Collectively, these findings demonstrate that cross-regional transport of biogenic oxidation products from the SEC region substantially enhances SOA production, especially for more aged or oxidized particles, in anthropogenically influenced urban clusters in the YRD region.

Biogenic-induced increase in SOA coatings on BC particles

The increased atmospheric oxidation and SOA production associated with biogenic-rich inflows are expected to substantially alter the physico-chemical properties of BC. To investigate these effects, we conducted detailed characterizations of BC-containing particles during the field campaign, focusing on the composition and oxidation of their coatings using an Aerodyne soot-particle aerosol mass spectrometry (SP-AMS). Figure 2 shows that biogenic-rich inflows led to pronounced changes in the chemical composition of BC coatings, most notably in the organic fraction. During biogenic-poor periods, organics accounted for 38% of coatings, whereas this fraction increased to 50% under biogenic-rich conditions (Fig. 2a). Among the organic coatings, the more oxidized oxygenated organic aerosol in BC-containing particles (MO-OOA_{BC}) showed the strongest enhancement, rising from 21% to 51% of total organic coatings (Extended Data Fig. 1c,e). Temporal variation analyses showed that BC particles with high coating amount originated predominantly from southeastern China, coinciding spatially with elevated MACR and MO-OOA_{BC} levels (Extended Data Figs. 1, 2 and 7). During these episodes, BC size distributions shifted towards larger diameters (Fig. 2b), reflecting increased coating accumulation. The mass ratio of MO-OOA_{BC} to BC core increased by up to a factor of four relative to biogenic-poor periods (Fig. 2c). A comparison between MO-OOA_{BC} and MO-OOA_{bulk} showed that an increasing fraction of aged SOA was coated on BC particles (Fig. 2d). In contrast, changes in other species, such as nitrate, sulfate and hydrocarbon-like organic aerosol (HOA), were minor or negligible.

As illustrated in Fig. 3a, the MO-OOA_{BC}-to-core mass ratio scaled exponentially with MACR, underscoring the link between biogenic oxidation products and SOA condensation onto BC. To assess how BC coatings evolved relative to the total particle population, we examined the MO-OOA_{BC}-to-MO-OOA_{bulk} ratio (Fig. 3b). This ratio also increased exponentially with MACR and was substantially higher during biogenic-rich periods, confirming that SOA formed under these conditions preferentially condensed to BC surfaces in the total particle population. The carbon oxidation state (OSc) of BC-containing particles, calculated from the atomic oxygen-to-carbon (O/C) and hydrogen-to-carbon (H/C) ratios (as $OSc = 2 \times O/C - H/C$) following Kroll et al. (ref. 35), likewise increased exponentially with MACR concentrations (Fig. 3c). In this study, the OSc values ranged on average from −1.4 to −0.5, slightly higher than those reported by Wang et al. (ref. 36) for urban Beijing in summer (−1.3 to −0.8) and by Lee et al. (ref. 8) in vehicular-influenced station in Fontana (−1.25 to −0.95). Concurrent increases in the MO-OOA_{BC} fraction indicate that biogenic-rich inflows enhanced the oxidation state of BC particles through the formation of highly oxidized secondary organic coatings. Figure 3d shows that OSc was positively correlated with the coating-to-core mass ratio (R_{BC}), accompanied by a concurrent increase in the fractional contribution of MO-OOA_{BC} within total coatings. This relationship indicates that as the oxidation state of BC-containing particles increased, both the total coating mass and the relative abundance of more oxidized SOA components also grew. Such a pattern is overall consistent with previous observations across diverse environments, including wintertime London[14], urban areas in California[8] and summertime Beijing[36].

Additional evidence was used to assess the biogenic-induced impacts on BC coating formation relative to the total particle population. Hydroxyl radical (OH) exposure ([OH]Δ*t*), an indicator of atmospheric oxidation processing derived from observed VOCs (Methods), was strongly correlated with ozone, both following exponential trends (Supplementary Fig. 6). The OSc shows good positive correlations with both ozone and the estimated photochemical age (Supplementary Fig. 6c), reinforcing the important role of atmospheric photochemical processes in BC ageing. Chemical transport model source apportionment indicated that ~70% of BC mass during biogenic-rich periods originated within the YRD region, with ~16% transported from southeastern China. SOA precursor analysis further showed that glyoxal and methylglyoxal received ~20% and ~32% of contributions from SEC biogenic emissions, respectively, while

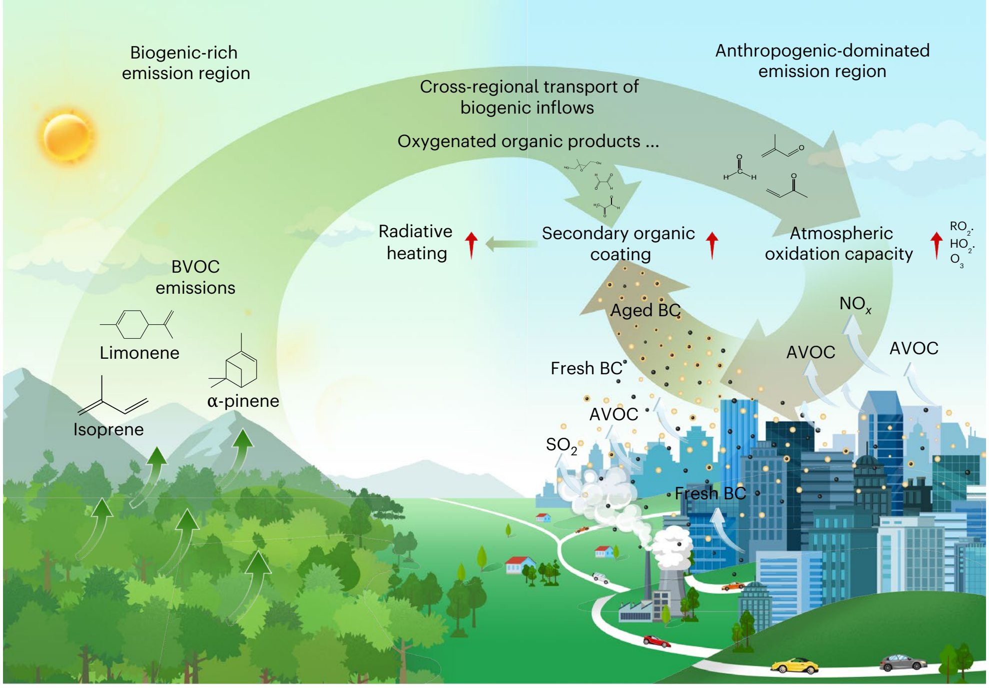

Fig. 5 | Conceptual framework of BC secondary organic coating formation in the total particle population under biogenic–anthropogenic interactions. Oxygenated products of BVOCs undergo cross-regional transport to areas with strong anthropogenic emissions, where BC coating is accelerated by the synergistic effects of enhanced atmospheric oxidation capacity and additional biogenic organics. These interactions play a critical role in regulating BC coating formation within the total particle population, thereby amplifying lensing enhancement and localized radiative heating.

isoprene epoxydiols (IEPOX) was ~56% regionally sourced. These biogenic-derived products may partly explain the enhanced SOA condensing onto BC surfaces. Supporting this interpretation, the SP-AMS fragment ion $C_5H_6O^+$ associated with isoprene-derived SOA[16], as shown in Supplementary Fig. 7, correlated well with both MACR ($r = 0.65$) and MO-OOA$_{BC}$ ($r = 0.90$). Importantly, aromatic hydrocarbons of anthropogenic origins[37] were lower during biogenic-rich periods (Extended Data Fig. 2c). Such reductions imply that the enhanced SOA coatings could potentially originate from oxidized aromatic precursors, whose availability in the gas phase was diminished under conditions of biogenic-enhanced atmospheric oxidation. Taken together, the exponential increases in BC coatings relative to the total particle population (Fig. 3b) and their oxidation state (Fig. 3c,d) pointed to enhanced atmospheric oxidation capacity—a boost by biogenic-rich inflows—as an important driver of BC coating formation. Under such conditions, SOA precursors from both local anthropogenic sources and regionally transported biogenic inflows probably condensed more efficiently onto BC, explaining the disproportionately greater coating growth on BC relative to the total particle population.

Radiative heating enhancement and atmospheric implications

Enhancement of BC light absorption due to the coating has been widely observed across diverse environments[11,13,38,39], with its magnitude varying substantially depending on the extent of particle ageing[12,40]. Here we assess the modulation of BC absorption by cross-regional biogenic inflows using observation-based and SP-AMS-constrained Mie modelling approaches to quantify the BC mass absorption cross section (MAC) values (Fig. 4a and Methods). Across the campaign, the average MAC at 880 nm was 5.1 ± 0.7 m^2 g^{-1}, which was comparable to the literature observations in the USA[6,13], but somewhat lower than values reported previously in summertime Nanjing (for example, 7.7 ± 2.7 m^2 g^{-1} at 781 nm) (ref. 41) and notably below values from western European cities such as Paris (8.6 m^2 g^{-1} at 880 nm) (refs. 39,42). During biogenic-rich periods, the MAC averaged 5.8 ± 0.8 m^2 g^{-1}, about 22% higher than the 4.7 ± 0.3 m^2 g^{-1} observed during biogenic-poor conditions. Mie model simulations yielded higher MAC values (7.9 ± 1.0 and 6.4 ± 0.7 m^2 g^{-1} for biogenic-rich and -poor periods, respectively), ~24% above observations yet consistent with the observed enhancement (Fig. 4a). Because absorption at 880 nm is barely sensitive to brown carbon, the observed increase in the MAC can be primarily attributed to the lensing effect[4,9,14].

Both observed and modelled MAC exhibited overall consistent increases with coating carbon oxidation state and photochemical age inferred from VOC ratios (Methods), consistent with the concurrent increase in coating amount (Fig. 3d). The modelled MAC values were systematically shifted upward by ~1–2 m^2 g^{-1} compared with the measurements. This bias was comparable to earlier reports in California[6,13] and probably reflects a tendency of core-shell Mie models to overestimate absorption enhancement when particle heterogeneity[38] and realistic morphologies[43–45] were not accounted for, particularly in the absence of single-particle BC measurements and morphology information in this study. Under biogenic-poor conditions, MAC showed only modest sensitivity to the oxidation state, whereas biogenic-rich inflows induced a markedly steeper increase, indicating that more extensively aged BC experienced absorption enhancement. Overall, these trends were comparable to those reported in relatively near-source urban environments[6,13]. These findings demonstrate a link between BC light absorption and the oxidation state of its organic coatings under photochemical ageing, with the oxidation state serving as a proxy for the extent of ageing[8,14]. To further quantify the atmospheric radiative effect of this enhanced absorption, we estimated BC-induced radiative heating (Fig. 4b) and forcing (Supplementary Fig. 8). During biogenic-rich periods, BC-induced radiative heating within the planetary boundary layer reached ~0.17 K d^{-1}, a 21% increase relative to uncoated BC (0.14 K d^{-1}). In biogenic-poor periods, heating was ~0.10 K d^{-1} compared to 0.09 K day^{-1} for uncoated BC, corresponding to an 11% enhancement. Similarly, BC-induced top-of-atmosphere shortwave radiative forcing increased from −1.01 W m^{-2} (uncoated) to −1.18 W m^{-2} during biogenic-rich periods and from −0.65 W m^{-2} to −0.68 W m^{-2} during biogenic-poor periods.

To capture the broader implications of this mechanism, Fig. 5 presents a conceptual framework illustrating how biogenic–anthropogenic interactions influence BC coating formation relative to the total particle population and radiative heating in downwind urban regions. BVOCs—emitted in areas of dense vegetation—are readily oxidized into a range of oxygenated products, including SOA precursors such as IEPOX[46], glyoxal and methylglyoxal[47] and OVOCs such as MACR, methyl vinyl ketone (MVK) and HCHO[37,48]. These products could be transported to urban receptor regions with high anthropogenic emissions, enhancing regional atmospheric oxidation capacity (for example, O_3, HO_2 and RO_2) while also supplying additional condensable organics. Accelerated BC coating formation arises from the synergistic effect of strengthened oxidation capacity and increased biogenic organics. Consequently, cross-regional biogenic–anthropogenic interactions exert a key role in regulating BC secondary organic coating formation within the total particle population, thereby intensifying lensing enhancement and radiative heating. This mechanism is probably widespread in regions where biogenic emissions intersect with anthropogenic pollution under conditions of regional transport. Under future carbon neutrality and climate mitigation strategies, which often involve large-scale afforestation and increased vegetative cover, BVOC emissions are expected to rise, potentially strengthening these cross-system interactions. Enhanced BC radiative forcing could contribute to additional warming and trigger feedbacks that further stimulate VOC emissions, complicating regional atmospheric chemistry.

Online content

Any methods, additional references, Nature Portfolio reporting summaries, source data, extended data, supplementary information, acknowledgements, peer review information; details of author contributions and competing interests; and statements of data and code availability are available at https://doi.org/10.1038/s41561-026-01922-5.

References

1. Bond, T. C. et al. Bounding the role of black carbon in the climate system: a scientific assessment. *J. Geophys. Res. Atmos.* **118**, 5380–5552 (2013).
2. Liu, D., He, C., Schwarz, J. P. & Wang, X. Lifecycle of light-absorbing carbonaceous aerosols in the atmosphere. *npj Clim. Atmos. Sci.* **3**, 40 (2020).
3. IPCC *Climate Change 2021: The Physical Science Basis* (Cambridge Univ. Press, 2021).
4. Jacobson, M. Z. Strong radiative heating due to the mixing state of black carbon in atmospheric aerosols. *Nature* **409**, 695–697 (2001).
5. Zhang, Y. et al. Extremely low-volatility organic coating leads to underestimation of black carbon climate impact. *One Earth* **6**, 158–166 (2023).
6. Cappa, C. D. et al. Radiative absorption enhancements due to the mixing state of atmospheric black carbon. *Science* **337**, 1078–1081 (2012).
7. Li, W. et al. Microphysical properties of atmospheric soot and organic particles: measurements, modeling, and impacts. *npj Clim. Atmos. Sci.* **7**, 65 (2024).
8. Lee, A. K. Y. et al. Formation of secondary organic aerosol coating on black carbon particles near vehicular emissions. *Atmos. Chem. Phys.* **17**, 15055–15067 (2017).
9. Fuller, K. A., Malm, W. C. & Kreidenweis, S. M. Effects of mixing on extinction by carbonaceous particles. *J. Geophys. Res.* **104**, 15941–15954 (1999).
10. Lack, D. A. & Cappa, C. D. Impact of brown and clear carbon on light absorption enhancement, single scatter albedo and absorption wavelength dependence of black carbon. *Atmos. Chem. Phys.* **10**, 4207–4220 (2010).
11. Peng, J. et al. Markedly enhanced absorption and direct radiative forcing of black carbon under polluted urban environments. *Proc. Natl Acad. Sci. USA* **113**, 4266–4271 (2016).
12. Fierce, L. et al. Constraining black carbon aging in global models to reflect timescales for internal mixing. *J. Adv. Model. Earth Syst.* **17**, e2024MS004471 (2025).
13. Cappa, C. D. et al. Light absorption by ambient black and brown carbon and its dependence on black carbon coating state for two California, USA, cities in winter and summer. *J. Geophys. Res. Atmos.* **124**, 1550–1577 (2019).
14. Liu, S. et al. Enhanced light absorption by mixed source black and brown carbon particles in UK winter. *Nat. Commun.* **6**, 8435 (2015).
15. Wang, J. et al. First chemical characterization of refractory black carbon aerosols and associated coatings over the Tibetan Plateau (4730 m a.s.l). *Environ. Sci. Technol.* **51**, 14072–14082 (2017).
16. Hu, W. W. et al. Characterization of a real-time tracer for isoprene epoxydiols-derived secondary organic aerosol (IEPOX-SOA) from aerosol mass spectrometer measurements. *Atmos. Chem. Phys.* **15**, 11807–11833 (2015).
17. Ying, Q., Li, J. & Kota, S. H. Significant contributions of isoprene to summertime secondary organic aerosol in eastern United States. *Environ. Sci. Technol.* **49**, 7834–7842 (2015).
18. Liaskoni, M. et al. The long-term impact of biogenic volatile organic compound emissions on urban ozone patterns over central Europe: contributions from urban and rural vegetation. *Atmos. Chem. Phys.* **24**, 13541–13569 (2024).
19. Shrivastava, M. et al. Urban pollution greatly enhances formation of natural aerosols over the Amazon rainforest. *Nat. Commun.* **10**, 1046 (2019).
20. Wang, P. et al. Updating biogenic volatile organic compound (BVOC) emissions with locally measured emission factors in South China and the effect on modeled ozone and secondary organic aerosol production. *J. Geophys. Res. Atmos.* **128**, e2023JD039928 (2023).
21. Gu, S., Guenther, A. & Faiola, C. Effects of anthropogenic and biogenic volatile organic compounds on Los Angeles air quality. *Environ. Sci. Technol.* **55**, 12191–12201 (2021).
22. Nagori, J. et al. Biogenic emissions and land–atmosphere interactions as drivers of the daytime evolution of secondary organic aerosol in the southeastern US. *Atmos. Chem. Phys.* **19**, 701–729 (2019).
23. Wang, N. et al. Typhoon-boosted biogenic emission aggravates cross-regional ozone pollution in China. *Sci. Adv.* **8**, eabl6166 (2022).
24. Wang, H., Liu, X., Wu, C. & Lin, G. Regional to global distributions, trends, and drivers of biogenic volatile organic compound emission from 2001 to 2020. *Atmos. Chem. Phys.* **24**, 3309–3328 (2024).
25. Yihui, D. & Chan, J. C. L. The east Asian summer monsoon: an overview. *Meteorol. Atmos. Phys.* **89**, 117–142 (2005).
26. Yang, K. et al. Increased variability of the western Pacific subtropical high under greenhouse warming. *Proc. Natl Acad. Sci. USA* **119**, e2120335119 (2022).
27. Zhao, Z. & Wang, Y. Influence of the West Pacific subtropical high on surface ozone daily variability in summertime over eastern China. *Atmos. Environ.* **170**, 197–204 (2017).
28. Wolfe, G. M. et al. Formaldehyde production from isoprene oxidation across NO_x regimes. *Atmos. Chem. Phys.* **16**, 2597–2610 (2016).
29. Marvin, M. R. et al. Impact of evolving isoprene mechanisms on simulated formaldehyde: An inter-comparison supported by in situ observations from SENEX. *Atmos. Environ.* **164**, 325–336 (2017).
30. Hewitt, C. N. et al. Ground-level ozone influenced by circadian control of isoprene emissions. *Nat. Geosci.* **4**, 671–674 (2011).

31. Wells, K. C. et al. Satellite isoprene retrievals constrain emissions and atmospheric oxidation. *Nature* **585**, 225–233 (2020).
32. Jacob, D. J. Heterogeneous chemistry and tropospheric ozone. *Atmos. Environ.* **34**, 2131–2159 (2000).
33. Zhang, Y. et al. Biogenic volatile organic compounds enhance ozone production and complicate control efforts: insights from long-term observations in Hong Kong. *Atmos. Environ.* **309**, 119917 (2023).
34. Li, Z. et al. Insights into the compositional differences of PM1 and PM2.5 from aerosol mass spectrometer measurements in Beijing, China. *Atmos. Environ.* **301**, 119709 (2023).
35. Kroll, J. H. et al. Carbon oxidation state as a metric for describing the chemistry of atmospheric organic aerosol. *Nat. Chem.* **3**, 133–139 (2011).
36. Wang, J. et al. Characterization of submicron organic particles in Beijing during summertime: comparison between SP-AMS and HR-AMS. *Atmos. Chem. Phys.* **20**, 14091–14102 (2020).
37. Ye, C. et al. Composition and evolution of reactive organic carbon in urban air. *Environ. Sci. Technol.* https://doi.org/10.1021/acs.est.4c10767 (2025).
38. Fierce, L. et al. Radiative absorption enhancements by black carbon controlled by particle-to-particle heterogeneity in composition. *Proc. Natl Acad. Sci. USA* **117**, 5196–5203 (2020).
39. Zanatta, M. et al. A European aerosol phenomenology-5: climatology of black carbon optical properties at 9 regional background sites across Europe. *Atmos. Environ.* **145**, 346–364 (2016).
40. Riemer, N., Ault, A. P., West, M., Craig, R. L. & Curtis, J. H. Aerosol mixing state: measurements, modeling, and impacts. *Rev. Geophys.* **57**, 187–249 (2019).
41. Ma, Y. et al. Mixing state and light absorption enhancement of black carbon aerosols in summertime Nanjing, China. *Atmos. Environ.* **222**, 117141 (2020).
42. Laborde, M. et al. Black carbon physical properties and mixing state in the European megacity Paris. *Atmos. Chem. Phys.* **13**, 5831–5856 (2013).
43. Wang, Y. et al. Improved representation of black carbon mixing structures suggests stronger direct radiative heating. *One Earth* https://doi.org/10.1016/j.oneear.2025.101311 (2025).
44. Liu, D. et al. The effect of complex black carbon microphysics on the determination of the optical properties of brown carbon. *Geophys. Res. Lett.* **42**, 613–619 (2015).
45. Romshoo, B. et al. Significant contribution of fractal morphology to aerosol light absorption in polluted environments dominated by black carbon (BC). *npj Clim. Atmos. Sci.* **7**, 87 (2024).
46. Xu, L. et al. Effects of anthropogenic emissions on aerosol formation from isoprene and monoterpenes in the southeastern United States. *Proc. Natl Acad. Sci. USA* **112**, 37–42 (2015).
47. Fu, T.-M. et al. Global budgets of atmospheric glyoxal and methylglyoxal, and implications for formation of secondary organic aerosols. *J. Geophys. Res. Atmos* **113**, D05 (2008).
48. Lyu, X. et al. Significant biogenic source of oxygenated volatile organic compounds and the impacts on photochemistry at a regional background site in South China. *Environ. Sci. Technol.* **58**, 20081–20090 (2024).

Yunjiang Zhang[1], Shijie Cui[1], Jingyi Li[1] ✉, Ming Wang[1], Xiaofeng Xu[2], Jiandong Wang[2], Jie Fang[1], Hanrui Lang[1], Bo Zheng[3], Sheng Zhong[4], Peng Sun[4], Haiwei Li[1], Yun Wu[1], Jianlin Hu[1], Junfeng Wang[1], Mindong Chen[1], Olivier Favez[5], Didier Hauglustaine[6], Philippe Ciais[6], Kaspar R. Daellenbach[7], André S. H. Prévôt[7] & Xinlei Ge[8] ✉

[1]Jiangsu Key Laboratory of Atmospheric Environment Monitoring and Pollution Control, School of Environmental Science and Engineering, Nanjing University of Information Science and Technology, Nanjing, China. [2]School of Atmospheric Physics, Nanjing University of Information Science and Technology, Nanjing, China. [3]Institute of Environment and Ecology, Tsinghua Shenzhen International Graduate School, Tsinghua University, Shenzhen, China. [4]Jiangsu Environmental Monitoring Center, Nanjing, China. [5]Institut National de l'Environnement Industriel et des Risques, Verneuil en Halatte, France. [6]Laboratoire des Sciences du Climat et de l'Environnement, CNRS-CEA-UVSQ, Université Paris-Saclay, Gif-sur-Yvette, France. [7]Laboratory of Atmospheric Chemistry, Paul Scherrer Institute, Villigen, Switzerland. [8]School of Energy and Environment, Southeast University, Nanjing, China. ✉e-mail: jingyili@nuist.edu.cn; xinlei@seu.edu.cn

Methods

Field measurements and data analysis

A comprehensive field campaign was conducted from 5 July to 2 August 2023 in urban Nanjing (32° 12′ N, 118° 42′ E), a major megacity in eastern China's economically developed region. The local climate exhibits strong seasonal variability, with prevailing southerly winds in summer that transport air masses from southeastern China—a region characterized by dense forest cover and high biogenic VOC emissions. These meteorological and emission features make Nanjing a representative receptor site for investigating biogenic–anthropogenic interactions. Locally, the site is situated near a major traffic corridor and is surrounded by industrial facilities, both of which serve as important sources of BC. Temporal variations in key meteorological parameters—relative humidity, air temperature, wind speed and direction, solar radiation and precipitation—are shown in Supplementary Fig. 9.

To investigate the chemical composition and oxidation state of BC-containing particles, we deployed a soot-particle aerosol mass spectrometer (SP-AMS, Aerodyne Research Inc.)[49] preceded by a $PM_{2.5}$ cyclone (URG-2000-30EN) to exclude coarse particles. Ambient air was first dried using a silica gel dryer to prevent moisture interference. The SP-AMS was configured to exclusively detect refractory black carbon (rBC) containing particles, using a 1,064 nm infrared laser vaporizer. The standard vaporizer was removed to avoid interference from non-refractory species. Instrument operation and calibration followed established protocols[50,51]. To increase sensitivity to low-concentration rBC, the instrument cycled between Particle Time-of-Flight (PToF, 30 s) and high-resolution time-of-flight (HR-ToF, 120 s) modes in an approximately 2.5-min cycle. Background correction and limit of detection were determined from a 60-min filtered air sample collected mid-campaign, with limit of detection defined as three times the standard deviation of background signals. Ionization efficiency (IE) and relative ionization efficiency (RIE) were calibrated using standards of ammonium nitrate, ammonium sulfate and 300 nm BC particles (REGAL 400 R, Cabot). A C_1^+/C_3^+ ratio of 0.65 was used to correct for interference from organic fragments in rBC quantification. Final RIE values were: 4.53 (NH_4), 1.10 (NO_3), 1.30 (SO_4), 0.17 (rBC), 1.3 (chloride, Chl) and 1.4 (organics, Org). Particle size calibration was performed using polystyrene latex spheres from 100 to 700 nm. A constant collection efficiency of 0.5 was applied, consistent with a prior study[52].

Complementary measurements of non-refractory $PM_{2.5}$ chemical composition were obtained using a time-of-flight aerosol chemical speciation monitor (ToF-ACSM, Aerodyne Research Inc.)[53] equipped with a $PM_{2.5}$ aerodynamic lens and standard vaporizer. The inlet was dried using a Nafion dryer (Perma Pure, MD-700-24F-3). The ToF-ACSM quantified major bulk aerosol chemical composition in NR-$PM_{2.5}$ constituents, including Org, NO_3, SO_4, NH_4 and Chl. Though this instrument provides robust bulk chemical profiles, it uses standard vaporization at 600 °C and electron impact ionization. Relative ionization efficiencies used were: 3.7 for NH_4, 0.92 for SO_4, 1.5 for Chl and a default of 1.4 for organics. A collection efficiency of 0.5 was used. Supplementary Fig. 10 shows the correlation between total NR-$PM_{2.5}$ from ToF-ACSM and gravimetrically determined $PM_{2.5}$ mass concentrations, revealing strong consistency ($r = 0.83$, slope = 0.85), validating the reliability of the ToF-ACSM data.

To evaluate the radiative impacts of BC, a seven-wavelength Aethalometer (AE33, Magee Scientific)[54,55] was used to measure $PM_{2.5}$ light absorption coefficient (b_{abs}). MAC at each wavelength was calculated by dividing the measured absorption by rBC mass concentrations from the SP-AMS (equation (1)). In this study, we used the MAC at 880 nm, a near-infrared wavelength minimally affected by brown carbon absorption, making it a reliable indicator of pure BC absorption[10]. Variations in MAC_{880} were therefore primarily attributed to the lensing effect associated with light-absorbing coatings on BC particles.

$$\mathrm{MAC_{BC}} = \frac{b_{abs}}{[\mathrm{rBC}]} \tag{1}$$

The Aethalometer infers absorption coefficients from the attenuation of light through particles collected on a filter tape[55]. However, this filter-based method is subject to several artefacts[56–59]. These include (1) multiple light scattering within the filter matrix[56–58], (2) the filter loading effect due to particle accumulation[55,57,60] and (3) cross sensitivity to scattering material deposited on the filter[61,62]. These artefacts can influence the apparent absorption relative to suspended particles. The attenuation signal (b_{ATN}) at each wavelength is related to the b_{abs} through equation (2):

$$b_{abs} = \frac{b_{ATN}}{C} \tag{2}$$

where C is the multiple-scattering parameter, which depends both on the filter tape used and on the optical properties of the deposited particles[56–58,62]. In the AE33 mode of Aethalometer, the loading effect is corrected online by the dual-spot technology, which applies real-time compensation based on the attenuation difference between two filter spots sampled at different flow rates[55]. In this study, aerosols were collected on two filter spots at 3.3 and 1.7 l min^{-1}, respectively, using the widely adopted M8060 filter tape[62]. For this tape, a default reference value ($C_{ref} = 1.39$) was pre-set in the instrument. However, we adjusted this value based on a harmonization factor ($H = 1.78$) obtained from our previous field intercomparison between the Aethalometer and photoacoustic extinctiometer during wintertime in urban Nanjing (Supplementary Fig. 11). This correction yielded a final C value of 2.47, which is overall comparable to values reported for previous studies[63,64]. To further minimize artefacts, potential interferences from relative humidity were reduced by installing a dryer upstream of the instrument inlet. It should be noted that C is not constant over time and is also influenced by the so-called 'cross sensitivity to scattering' effect[61,62], which can be parametrized by equation (3).

$$b_{abscorr} = \frac{b_{ATN}}{C} - m_s \times b_{scatt} \tag{3}$$

where $b_{abscorr}$ is the corrected absorption coefficient, b_{scatt} is the scattering coefficient and m_s is describing the additional attenuation due to the presence of scattering material in the filter. In this study, b_{scatt} was estimated using $PM_{2.5}$ chemical composition from the ToF-ACSM, based on a regression model (Supplementary Fig. 12) obtained from collocated photoacoustic extinctiometer scattering measurements at 870 nm and a $PM_{2.5}$ quadrupole-ACSM chemical composition during autumn in urban Nanjing[65]. Assuming a maximum upper bound of m_s value 2.5% (ref. 55), the resulting potential uncertainty in the MAC value was estimated at ~11% (Supplementary Fig. 13).

VOCs measurements and photochemical age estimation

Ambient concentrations of selected VOCs, including o-xylene, ethylbenzene, isoprene, acetylene and methacrolein, which were measured hourly using an online dual-column gas chromatograph coupled with mass spectrometer and flame ionization detector (GC-MS/FID) system[66]. OH exposure ([OH]Δt) of observed air masses was estimated using the VOCs ratio method, assuming an ideal, isolated well-mixed air parcel unaffected by mixing or fresh emissions (equation (4)).

$$[\mathrm{OH}]\Delta t = \frac{1}{k_{\mathrm{HC_1}} - k_{\mathrm{HC_2}}} \times \left(\ln\left(\frac{\mathrm{HC_1}}{\mathrm{HC_2}}\right)_{t_E} - \ln\left(\frac{\mathrm{HC_1}}{\mathrm{HC_2}}\right)_{t_M} \right) \tag{4}$$

where HC_1 and HC_2 are two hydrocarbons with substnatially different reactivities, which should either have similar sources or exhibit relatively consistent ratios across different emission sources[67,68]. $k_{\mathrm{HC_1}}$ and $k_{\mathrm{HC_2}}$ represent the reaction rate constants of HC_1 and HC_2 with the OH radical, respectively. The ratios $\left(\frac{\mathrm{HC_1}}{\mathrm{HC_2}}\right)_{t_E}$ and $\left(\frac{\mathrm{HC_1}}{\mathrm{HC_2}}\right)_{t_M}$ correspond to the emission and measured ratios of HC_1/HC_2. In this study, o-xylene and ethylbenzene were chosen to calculate $[OH]\Delta t$ due to their common sources, differing reaction rates with OH and suitability for first-order kinetic analysis. The emission ratio of o-xylene/ethylbenzene was estimated to be 0.91, based on the 95th percentile of measured o-xylene/ethylbenzene ratios (Supplementary Fig. 14). Assuming the average OH radical concentration of 1.5×10^6 molecule cm^{-3} based on measurements conducted in the YRD region during the summer of 2019[69], the photochemical age (Δt) was estimated. Further methodological details can be found in refs. 48,67,68. To apportion sources of MACR—a key oxygenated VOC associated with isoprene oxidation—we employed a nonlinear source apportionment framework based on the approach of ref. 67. Observed MACR was partitioned into four components: anthropogenic primary emissions, anthropogenic secondary formation, biogenic sources and background. Isoprene was used as a tracer for biogenic emissions and acetylene as a marker for anthropogenic primary sources.

Additionally, in situ measurements of NO_2 and O_3 were continuously recorded at the field site using standard online gas analysers. Meteorological variables—including temperature, relative humidity, wind speed and direction and rainfall—were measured using an automatic weather station co-located with the sampling platform. In addition, hourly ground-level air quality data for O_3, NO_2 and $PM_{2.5}$ were obtained from the National Environmental Monitoring Center of China (https://air.cnemc.cn:18007/). These data were used to evaluate the regional representativeness of our measurements and to extend our analysis to broader spatial scales.

Source apportionment of OA

High-resolution SP-AMS data were processed using the standard ToF-AMS software suite (SQUIRREL v1.59D and PIKA v1.19D) within the Igor Pro. Mass concentrations of rBC and its associated coatings were obtained by fitting V-mode mass spectra, whereas size distributions were derived from PToF data and normalized by mass. The size distribution of rBC particles was quantified using the minimally interfering C_2^+ fragment ion (m/z 24), following established protocols[70,71]. Elemental ratios of organics, including O/C, H/C, nitrogen-to-carbon (N/C) and organic-mass-to-organic-carbon ratio (OM/OC), were calculated from high-resolution mass spectra using both the traditional Aiken-Ambient (A-A) method[72] and the improved I-A method[73]. Consistent results were obtained from both approaches; the I-A method was ultimately adopted, yielding average ratios of O/C = 0.33, H/C = 1.5, and OM/OC = 1.6.

To identify major OA sources, Positive Matrix Factorization (PMF) was applied to high-resolution organic spectra using the PMF Evaluation Tool[74], following diagnostic criteria outlined by ref. 75. A five-factor solution was selected, comprising two primary organic aerosol (POA) factors—hydrocarbon-like OA (HOA_{BC}) and rBC-rich OA—and three SOA factors: a locally derived low-oxidation oxygenated OA ($LO\text{-}OOA_{BC}$ I), a regionally transported low-oxidation OA ($LO\text{-}OOA_{BC}$ II) and a more oxidized OA ($MO\text{-}OOA_{BC}$). Supplementary Fig. 15 presents the mass spectral profiles and diurnal variations of these five factors, demonstrating their distinct signatures and temporal behaviour consistent with known POA and SOA sources. Additional PMF diagnostics supporting factor separation and robustness are provided in Supplementary Fig. 16.

Bulk OA source apportionment was also performed on ToF-ACSM measurements, yielding five factors: HOA_{bulk}, COA_{bulk}, oxygenated COA_{bulk}, $LO\text{-}OOA_{bulk}$ and $MO\text{-}OOA_{bulk}$. Supplementary Fig. 17 shows the mass spectra and diurnal cycles of these factors, consistent with established POA and SOA signatures. Detailed diagnostics results from the PMF analysis are shown in Supplementary Fig. 18. COA-related factors were not observed in SP-AMS data, which aligns with prior findings in many urban environments[6,8,13,14,52,70,76], indicating that cooking emissions are generally not associated with rBC-containing particles.

To assess the plausibility of the identified factors, a series of cross-comparisons was conducted (Supplementary Fig. 19). The bulk HOA factor resolved from ToF-ACSM displayed a strong correlation with NO_2, consistent with its traffic-related origin, thus validating the source attribution. Further comparison between HOA_{bulk} and HOA_{BC} revealed a good correlation ($r = 0.54$, slope = 0.85), indicating that an important fraction of HOA is internally mixed with BC. This result is consistent with observations in other urban locations[6,14,52,70,76], where traffic emissions are known to co-emit BC and POA. Similarly, the $MO\text{-}OOA_{BC}$ and $MO\text{-}OOA_{bulk}$ showed a strong correlation ($r = 0.80$, slope = 0.28), indicating a shared source, albeit with lower mixing efficiency with BC than HOA. $MO\text{-}OOA_{bulk}$ also exhibited good correlation with sulfate, supporting its attribution to regional secondary formation processes common in summer urban atmospheres. For the LO-OOA factor, two distinct BC-containing components ($LO\text{-}OOA_{BC}$ I and $LO\text{-}OOA_{BC}$ II) were resolved in SP-AMS data, probably reflecting different secondary formation pathways. In contrast, only one composite $LO\text{-}OOA_{bulk}$ factor was identified in the ToF-ACSM analysis, possibly due to its lower chemical resolution. A comparison of the summed $LO\text{-}OOA_{BC}$ I and II with the $LO\text{-}OOA_{bulk}$ showed higher correlation than comparisons with either individual factor, suggesting that the $LO\text{-}OOA_{bulk}$ represents a combined signature of both BC-containing LO-OOA components. This consistency supports the robustness of the factor attribution across instruments.

BC absorption calculation with the Mie model

To simulate the influence of non-BC coating materials on the light absorption of BC-containing particles associated with the lensing effect, we employed a core-shell Mie model constrained by field observations. BC-containing particles were treated as spherical cores surrounded by concentric coatings of non-BC material, with the coating mass assumed to be homogeneously distributed across all BC particles. Parameters describing the BC core size distribution and coating mass were derived from the SP-AMS measurements. The relative coating thickness, expressed as the ratio of particle radius ($r_{particle}$) to core (r_{core}), was calculated using the method developed by Cappa et al.[6]:

$$\frac{r_{particle}}{r_{core}} = \sqrt[3]{\frac{m_{coating}}{\rho_{coating}}\frac{\rho_{BC}}{m_{BC}} + 1} = \sqrt[3]{R_{BC}\frac{\rho_{BC}}{\rho_{coating}}}, \tag{5}$$

where m_{BC} *and* $m_{coating}$ are the measured mass concentrations of BC cores and coatings, respectively, and ρ denotes species-specific densities. R_{BC} refers to the ratio of $m_{coating}$ to m_{BC}. We used densities of 1.8 g cm^{-3} for BC, 1.7 g cm^{-3} for inorganics, 1.0 g cm^{-3} for HOA, 1.4 g cm^{-3} for OOA factors[6]. Optical properties were parameterized using a complex refractive index of 1.88 + 0.8i for the BC core[6] and 1.5 + 0i for the non-BC shell[77] at 880 nm.

Particle time-of-flight (pToF) measurements were conducted using the SP-AMS to determine the vacuum aerodynamic diameter (D_{va}) of black carbon (BC)-containing particles[49]. Individual pToF traces were obtained for different chemical species within the BC-containing aerosols, including BC, OA, sulfate, nitrate, ammonium and chloride. Although the SP-AMS primarily detects BC-containing particles, the observed D_{va} for each particle reflects contributions from both the BC core and its non-refractory coating materials ($NR\text{-}PM_{BC}$). Hence, the pToF-derived size distribution represents a combination of these two components. Following Cappa et al. (ref. 6), the measured D_{va} can be converted to the volume-equivalent diameter of the BC core ($D_{ve,BC}$) using equation (6):

$$D_{ve,BC} = \left(\frac{\rho_0}{\rho_p}x_v D_{va}\right)\left(\frac{\rho_p}{\rho_{p,BC}}f_{BC}\right)^{\frac{1}{3}} \tag{6}$$

where ρ_p is the effective density of the BC-containing particle (including both BC and coating materials), ρ_0 is the reference density (1 g cm^{-3}) and x_v is the dynamic shape factor that accounts for particle non-sphericity in drag force calculations. The value of x_v equals 1 for spherical particles and exceeds 1 for non-spherical particles. In this study, because no direct measurements of particle morphology were available, aerosol particles were assumed to be spherical and a shape factor $x_v = 1$ was applied.

Satellite observation and data analysis

Daily measurements of column densities of nitrogen dioxide (NO_2) and HCHO were acquired from the TROPOMI satellite sensor (Level 2 Product). To ensure the quality of the data, we applied specific quality assurance criteria, requiring values larger than 0.75 for NO_2 and larger than 0.5 for HCHO when selecting data pixels. Finally, the typical pixel size of the spectral bands in the TROPOMI data (approximately 7 × 3.5 km^2) was aggregated to match the standard grids of the meteorological field (0.25° × 0.25°).

Tropospheric ozone formation exhibits a nonlinear response to its precursors and can be broadly categorized into three sensitivity regimes: VOC-limited, NO_x-limited and transitional (or mixed) regimes[78]. The ratio of HCHO to NO_2 column densities—commonly referred to as the formaldehyde-to-NO_2 ratio (FNR)—serves as a widely adopted indicator of ozone formation sensitivity in satellite-based diagnostics[78,79]. In this study, ozone sensitivity regimes during summer 2023 were classified based on the mean (FNR_{avg}) and standard deviation (FNR_{sd}) of daily FNR values[78,80]. Specifically, regions were diagnosed as:

(1) VOC limited when $FNR_{avg} < 4.0$ and $FNR_{avg} + FNR_{sd} < 6.0$;
(2) NO_x limited when $FNR_{avg} > 4.0$ and $FNR_{avg} - FNR_{sd} > 2.0$;
(3) Transitional otherwise.

Backward trajectory analysis

To identify the geographic origins and transport pathways of air masses influencing the sampling site, 48-h backward trajectories were calculated at 100 m above ground level using the Hybrid Single-Particle Lagrangian Integrated Trajectory (HYSPLIT) model[81], with meteorological input from the Global Data Assimilation System (GDAS). Trajectories were initiated at hourly intervals throughout the campaign to ensure high temporal resolution. To assess the potential source regions associated with elevated levels of SOA and oxygenated VOCs such as MACR, we applied the concentration-weighted trajectory (CWT) approach[82].

Chemical transport model simulations

The Community Multiscale Air Quality model (CMAQ v5.2)[83,84], coupled with a modified SAPRC07tic chemical mechanism and the AERO6i aerosol module, was used to simulate the evolution of air pollutants over eastern China from 1 July to 1 August 2023. This model has been widely adopted in simulating SOA formation in the USA, China and other Asian countries with acceptable performances[83,85,86]. The modelling domain (Supplementary Fig. 20) has a horizontal resolution of 36 km × 36 km, with 18 vertical layers extending from the surface up to approximately 21 km above ground level. A precursor-tagging approach was incorporated into the gas-phase mechanism to quantify the formation of SOA from emissions originating in different regions[87]. A unique label was assigned to all precursor VOCs emitted from a specific region and to their subsequent oxidation products (for example, VOC_X1 + OH → Prod1_X1 + Prod2_X1 + ...), enabling the distinction of SOA formed from emissions in the targeted region from that generated elsewhere within the simulation domain. A similar tagging approach was applied to the emissions of BC from different regions for source apportionment. To better represent SOA formation from monoterpene oxidation, the model was updated with a six-bin volatility basis set parameterization[88]. Additionally, an enhancement in NO_2 heterogeneous uptake by aerosols under high ionic strength conditions was also taken into account[89]. To assess the influence of biogenic and anthropogenic VOC emissions from the SEC region on the atmospheric oxidation capacity in the YRD, another two sensitivity scenarios were designed in which the respective SEC BVOC and AVOC emissions were set to zero (Supplementary Fig. 20), while all other emissions and meteorological fields were kept identical to those in the base case.

Meteorological fields were generated using the Weather Research and Forecasting model version 4.2.1, with initial and boundary conditions from the National Centers for Environmental Prediction (NCEP) Final (FNL) Operational Model Global Tropospheric Analyses dataset. Anthropogenic emissions were derived from the Multi-resolution Emission Inventory for China (MEICv1.4)[90,91] for mainland China and from the Regional Emission inventory in ASia (REASv3.2.1) for other regions of the domain[92]. Biogenic emissions were generated by the Model of Emissions of Gases and Aerosols from Nature (MEGANv2.1). Open biomass burning emissions were obtained from the Fire INventory from NCAR (FINNv2.5)[93]. The boundary and Initial conditions were based on the default CMAQ profiles. The first five days were treated as spin-up and excluded from the analysis.

Supplementary Fig. 21 shows time series comparisons of simulated and observed concentrations for OA, SOA and ozone. The model captures the general diurnal and episodic variations for most species. Quantitative statistical metrics show reasonable agreement across variables. For example, the root mean square error for OA, SOA and O_3 were 6.6 μg m^{-3}, 6.2 μg m^{-3} and 49.3 μg m^{-3}, respectively, while the index of agreement exceeded 0.51 for most species. Supplementary Fig. 22 presents spatial comparisons for O_3, NO_2 and $PM_{2.5}$ across eastern China. Overall, the spatial distribution of the simulated values is in excellent agreement with the observed concentrations. The model successfully reproduces the major spatial gradients, including urban–rural contrasts and regional pollution hotspots. These evaluation results collectively suggest that the model provides a reasonable representation of both temporal dynamics and spatial patterns of key atmospheric pollutants. The adequate reproduction of SOA and OA variability supports the credibility of the model in capturing SOA formation and chemical ageing processes, thus providing a robust foundation for interpreting the biogenic influence on urban air quality.

Simulation of radiative heating rate

To assess the contribution of BC to atmospheric radiative heating and forcing, we performed radiative transfer simulations using the Santa Barbara DISORT Atmospheric Radiative Transfer (SBDART) model[94,95] under two contrasting scenarios. In the BC-present case, the aerosol optical depth attributable to BC was derived from ground-based Aethalometer absorption measurements, with vertical attenuation assumed to follow an exponential decay profile characterized by a scale height of 1.5 km (ref. 96). The single scattering albedo and asymmetry parameter were specified as 0.2088 and 0.366, respectively, based on values from the optical properties of aerosols and clouds (OPAC) soot aerosol optical property database[97]. To isolate BC-driven radiative effects from brown carbon at low-wavelength bands and maintain consistency with our absorption analysis, absorption coefficients at other wavelengths were estimated from the 880 nm Aethalometer measurements. The absorption Ångström exponent of 1 (ref. 98) was obtained via spectral fitting of multi-wavelength BC absorption data. It should be noted that these simulations account solely for BC-induced heating, excluding contributions from other light-absorbing aerosols.

We used SBDART to simulate shortwave heating rate profiles and top-of-atmosphere (TOA) shortwave radiative fluxes over the study period under clear-sky conditions. Meteorological input fields, including 3-hourly vertical profiles of temperature and humidity, were obtained from the MERRA2 reanalysis product. Simulations were conducted for both BC-present and BC-absent scenarios, with all other parameters (for example, surface albedo, non-BC aerosol properties and atmospheric profiles) held constant. The BC-absent scenario allowed isolation of the radiative effects attributable solely to BC. Radiative fluxes were calculated at 3-h intervals for each vertical layer, and corresponding heating rate profiles were derived. The net atmospheric heating induced by BC was determined as the difference between BC-present and BC-free heating rates. In this study, we focus on the boundary-layer heating rate, defined as the mean shortwave heating rate from the surface to 1 km altitude. Similarly, BC-induced direct radiative forcing at the TOA was calculated as the difference in upward radiative fluxes between the two scenarios (that is, BC-present versus BC-free). To further evaluate the role of absorption enhancement from BC coatings, we performed a sensitivity analysis in which uncoated BC light absorption coefficients were estimated using SP-AMS-measured rBC mass concentrations and a mass-normalized absorption cross section of 7.5 ± 1.2 $m^2 g^{-1}$ at 550 nm for uncoated particles[99]. Heating rates and radiative forcing values for uncoated BC were then calculated using the same SBDART framework, allowing comparison with the coated-BC results to quantify the contribution of lensing effects. Finally, sensitivity tests showed that uncertainties in the Aethalometer absorption scale nearly linearly with simulated BC-induced heating and forcing, implying that instrument uncertainty translates proportionally into the radiative estimates.

Data availability

The datasets supporting the findings of this study, including those used in the main-text figures and Extended Data figures, are available via Zenodo at https://doi.org/10.5281/zenodo.17841634 (ref. 100). The ground-level air quality data were obtained from the National Environmental Monitoring Center of China (https://air.cnemc.cn:18007/). The TROPOMI satellite data were accessible at https://dataspace.copernicus.eu/. The back-trajectory data were from the Global Data Assimilation System (GDAS), which can be downloaded at https://www.ready.noaa.gov/data/archives/gdas1/. Additional data are available upon request.

Code availability

The ToF-AMS software used for SP-AMS data analysis is available at https://cires1.colorado.edu/jimenez-group/ToFAMSResources/ToFSoftware/. The PMF analysis was performed using the PET PMF toolkit, available at https://cires1.colorado.edu/jimenez-group/wiki/index.php/PMF-AMS_Analysis_Guide. ToF-ACSM data were processed with Tofware, which is available from its distributors, Tofwerk AG and Aerodyne Research Inc. The source code of the CMAQ model can be obtained via Github at https://github.com/USEPA/CMAQ/tree/5.2. Backward trajectory simulations were conducted using the HYSPLIT model, available at https://www.ready.noaa.gov/HYSPLIT.php. The CWT analyses were implemented using Igor-based code provided by the ZeFir project at https://sites.google.com/site/zefirproject/download. Radiative heating calculations were performed using SBDART, available via Github at https://github.com/paulricchiazzi/SBDART.

References

49. Onasch, T. B. et al. Soot particle aerosol mass spectrometer: development, validation, and initial application. *Aerosol Sci. Technol.* **46**, 804–817 (2012).
50. Lee, A. K. Y., Willis, M. D., Healy, R. M., Onasch, T. B. & Abbatt, J. P. D. Mixing state of carbonaceous aerosol in an urban environment: single particle characterization using the soot particle aerosol mass spectrometer (SP-AMS). *Atmos. Chem. Phys.* **15**, 1823–1841 (2015).
51. Willis, M. D. et al. Quantification of black carbon mixing state from traffic: implications for aerosol optical properties. *Atmos. Chem. Phys.* **16**, 4693–4706 (2016).
52. Cui, S. et al. Chemical properties, sources and size-resolved hygroscopicity of submicron black-carbon-containing aerosols in urban Shanghai. *Atmos. Chem. Phys.* **22**, 8073–8096 (2022).
53. Fröhlich, R. et al. The ToF-ACSM: a portable aerosol chemical speciation monitor with TOFMS detection. *Atmos. Meas. Tech.* **6**, 3225–3241 (2013).
54. Drinovec, L. et al. A dual-wavelength photothermal aerosol absorption monitor: design, calibration and performance. *Atmos. Meas. Tech.* **15**, 3805–3825 (2022).
55. Drinovec, L. et al. The 'dual-spot' Aethalometer: an improved measurement of aerosol black carbon with real-time loading compensation. *Atmos. Meas. Tech.* **8**, 1965–1979 (2015).
56. Collaud Coen, M. et al. Minimizing light absorption measurement artifacts of the Aethalometer: evaluation of five correction algorithms. *Atmos. Meas. Tech.* **3**, 457–474 (2010).
57. Weingartner, E. et al. Absorption of light by soot particles: determination of the absorption coefficient by means of aethalometers. *J. Aerosol Sci.* **34**, 1445–1463 (2003).
58. Ajtai, T. et al. Diurnal variation of aethalometer correction factors and optical absorption assessment of nucleation events using multi-wavelength photoacoustic spectroscopy. *J. Environ. Sci.* **83**, 96–109 (2019).
59. Yus-Díez, J. et al. Characterization of filter photometer artifacts in soot and dust measurements—laboratory and ambient experiments using a traceably calibrated aerosol absorption reference. *Atmos. Meas. Tech.* **18**, 3073–3093 (2025).
60. Lack, D. A. et al. Bias in filter-based aerosol light absorption measurements due to organic aerosol loading: evidence from ambient measurements. *Aerosol Sci. Technol.* **42**, 1033–1041 (2008).
61. Drinovec, L. et al. The filter-loading effect by ambient aerosols in filter absorption photometers depends on the coating of the sampled particles. *Atmos. Meas. Tech.* **10**, 1043–1059 (2017).
62. Yus-Díez, J. et al. Determination of the multiple-scattering correction factor and its cross-sensitivity to scattering and wavelength dependence for different AE33 Aethalometer filter tapes: a multi-instrumental approach. *Atmos. Meas. Tech.* **14**, 6335–6355 (2021).
63. Savadkoohi, M. et al. The variability of mass concentrations and source apportionment analysis of equivalent black carbon across urban Europe. *Environ. Int.* **178**, 108081 (2023).
64. Wu, L. et al. Field comparison of dual- and single-spot Aethalometers: equivalent black carbon, light absorption, Ångström exponent and secondary brown carbon estimations. *Atmos. Meas. Tech.* **17**, 2917–2936 (2024).
65. Zhang, Y. et al. Field characterization of the PM2.5 aerosol chemical speciation monitor: insights into the composition, sources, and processes of fine particles in eastern China. *Atmos. Chem. Phys.* **17**, 14501–14517 (2017).
66. Wang, M. et al. Development and validation of a cryogen-free automatic gas chromatograph system (GC-MS/FID) for online measurements of volatile organic compounds. *Anal. Methods* **6**, 9424–9434 (2014).
67. de Gouw, J. A. et al. Budget of organic carbon in a polluted atmosphere: results from the New England Air Quality Study in 2002. *J. Geophys. Res. Atmos.* **110**, D16 (2005).
68. Shao, M. et al. Volatile organic compounds measured in summer in Beijing and their role in ground-level ozone formation. *J. Geophys. Res. Atmos* **114**, D2 (2009).
69. Zhai, T. et al. Elucidate the formation mechanism of particulate nitrate based on direct radical observations in the Yangtze River Delta summer 2019. *Atmos. Chem. Phys.* **23**, 2379–2391 (2023).
70. Wang, J. et al. Characterization of black carbon-containing fine particles in Beijing during wintertime. *Atmos. Chem. Phys.* **19**, 447–458 (2019).
71. Collier, S. et al. Influence of emissions and aqueous processing on particles containing black carbon in a polluted urban environment: insights from a soot particle-aerosol mass spectrometer. *J. Geophys. Res. Atmos.* **123**, 6648–6666 (2018).

72. Aiken, A. C. et al. O/C and OM/OC ratios of primary, secondary, and ambient organic aerosols with high-resolution time-of-flight aerosol mass spectrometry. *Environ. Sci. Technol.* **42**, 4478–4485 (2008).
73. Canagaratna, M. R. et al. Chemical compositions of black carbon particle cores and coatings via soot particle aerosol mass spectrometry with photoionization and electron ionization. *J. Phys. Chem. A* **119**, 4589–4599 (2015).
74. Ulbrich, I. M., Canagaratna, M. R., Zhang, Q., Worsnop, D. R. & Jimenez, J. L. Interpretation of organic components from positive matrix factorization of aerosol mass spectrometric data. *Atmos. Chem. Phys.* **9**, 2891–2918 (2009).
75. Zhang, Q. et al. Understanding atmospheric organic aerosols via factor analysis of aerosol mass spectrometry: a review. *Anal Bioanal Chem* **401**, 3045–3067 (2011).
76. Wu, Y. et al. Characterization of size-resolved hygroscopicity of black carbon-containing particle in urban environment. *Environ. Sci. Technol.* **53**, 14212–14221 (2019).
77. Liu, D. et al. Black-carbon absorption enhancement in the atmosphere determined by particle mixing state. *Nat. Geosci.* **10**, 184–188 (2017).
78. Ren, J., Guo, F. & Xie, S. Diagnosing ozone–NOx–VOC sensitivity and revealing causes of ozone increases in China based on 2013–2021 satellite retrievals. *Atmos. Chem. Phys.* **22**, 15035–15047 (2022).
79. Sillman, S. The use of NO_y, H_2O_2, and HNO_3 as indicators for ozone-NO_x -hydrocarbon sensitivity in urban locations. *J. Geophys. Res. Atmos.* **100**, 14175–14188 (1995).
80. Jin, X. & Holloway, T. Spatial and temporal variability of ozone sensitivity over China observed from the ozone monitoring instrument. *J. Geophys. Res. Atmos.* **120**, 7229–7246 (2015).
81. Draxler, R. R. & Rolph, G. D. HYSPLIT (HYbrid Single-Particle Lagrangian Integrated Trajectory) model access. *NOAA Air Resources Laboratory* http://www.arl.noaa.gov/ready/hysplit4.html (2003).
82. Petit, J. E., Favez, O., Albinet, A. & Canonaco, F. A user-friendly tool for comprehensive evaluation of the geographical origins of atmospheric pollution: wind and trajectory analyses. *Environ. Modell. Softw.* **88**, 183–187 (2017).
83. Murphy, B. N. et al. Semivolatile POA and parameterized total combustion SOA in CMAQv5.2: impacts on source strength and partitioning. *Atmos. Chem. Phys.* **17**, 11107–11133 (2017).
84. Xie, Y. et al. Understanding the impact of recent advances in isoprene photooxidation on simulations of regional air quality. *Atmos. Chem. Phys.* **13**, 8439–8455 (2013).
85. Li, Y., Carlton, A. G. & Shiraiwa, M. Diurnal and seasonal variations in the phase state of secondary organic aerosol material over the contiguous US simulated in CMAQ. *ACS Earth Space Chem.* **5**, 1971–1982 (2021).
86. Rooney, B. et al. Impacts of household sources on air pollution at village and regional scales in India. *Atmos. Chem. Phys.* **19**, 7719–7742 (2019).
87. Li, L. et al. Modelling air quality during the EXPLORE-YRD campaign – part II. Regional source apportionment of ozone and PM2.5. *Atmos. Environ.* **247**, 118063 (2021).
88. Appel, K. W. et al. The Community Multiscale Air Quality (CMAQ) model versions 5.3 and 5.3.1: system updates and evaluation. *Geosci. Model Dev.* **14**, 2867–2897 (2021).
89. Gen, M. et al. Rapid hydrolysis of NO_2 at high ionic strengths of deliquesced aerosol particles. *Environ. Sci. Technol.* **58**, 7904–7915 (2024).
90. Zheng, B. et al. Trends in China's anthropogenic emissions since 2010 as the consequence of clean air actions. *Atmos. Chem. Phys.* **18**, 14095–14111 (2018).
91. Zheng, B. et al. Changes in China's anthropogenic emissions and air quality during the COVID-19 pandemic in 2020. *Earth Syst. Sci. Data* **13**, 2895–2907 (2021).
92. Kurokawa, J. & Ohara, T. Long-term historical trends in air pollutant emissions in Asia: Regional Emission inventory in ASia (REAS) version 3. *Atmos. Chem. Phys.* **20**, 12761–12793 (2020).
93. Wiedinmyer, C. et al. The fire inventory from NCAR version 2.5: an updated global fire emissions model for climate and chemistry applications. *Geosci. Model Dev.* **16**, 3873–3891 (2023).
94. Ricchiazzi, P., Yang, S., Gautier, C. & Sowle, D. SBDART: a research and teaching software tool for plane-parallel radiative transfer in the Earth's amosphere. *Bull. Am. Meteorol. Soc.* **79**, 2101–2114 (1998).
95. Barnard, J. C. & Powell, D. M. A comparison between modeled and measured clear-sky radiative shortwave fluxes in Arctic environments, with special emphasis on diffuse radiation. *J. Geophys. Res. Atmos.* **107**, ACL 9-1–ACL 9-10 (2002).
96. Xu, X., Qiu, J., Xia, X., Sun, L. & Min, M. Characteristics of atmospheric aerosol optical depth variation in China during 1993–2012. *Atmos. Environ.* **119**, 82–94 (2015).
97. Hess, M., Koepke, P. & Schult, I. Optical properties of aerosols and clouds: the software package OPAC. *Bull. Am. Meteorol. Soc.* **79**, 831–844 (1998).
98. Lack, D. A. & Langridge, J. M. On the attribution of black and brown carbon light absorption using the Ångström exponent. *Atmos. Chem. Phys.* **13**, 10535–10543 (2013).
99. Bond, T. C. & Bergstrom, R. W. Light absorption by carbonaceous particles: an investigative review. *Aerosol Sci. Technol.* **40**, 27–67 (2006).
100. Zhang, Y. Data for 'Urban black-carbon radiative heating intensified by biogenic-anthropogenic interactions'. *Zenodo* https://doi.org/10.5281/zenodo.17841634 (2025).

Acknowledgements

This study was supported by the National Natural Science Foundation of China (grant 42207124 to Y.Z.), the Natural Science Foundation of Jiangsu Province (grant BK20210663 to Y.Z.), the National Natural Science Foundation of China (grant 41705102 to J.L.) and (grant 42377100 to X.G.) and the National Key Research and Development Program of China (grant 2023YFC3706200 to M.W.) and (grant 2022YFC3701000 to J.H.). We also gratefully acknowledge Z. Zhang for his assistance with the optical simulations of black carbon.

Author contributions

Y.Z., J.L. and X.G. conceived the study and designed the research framework. Y.Z., S.C., S.Z. and P.S. conducted the field measurements and performed data validation. Y.Z. and J.F. analysed satellite observations. Y.Z. and X.X. carried out the radiative heating simulations, Y.Z. and Jiandong Wang performed aerosol optical simulations and J.L. conducted the atmospheric chemical transport modelling. Y.Z. and H. Lang performed the air mass trajectory analysis. Y.Z., J.F. and H. Lang processed the national air quality monitoring data. Y.Z. integrated all datasets, performed the analyses and wrote the original manuscript. J.L., M.W., X.X., Jiandong Wang, B.Z., H. Li, Y.W., J.H., Junfeng Wang, M.C., O.F., D.H., P.C., K.R.D., A.S.H.P. and X.G. provided critical comments and contributed to manuscript revisions. All authors contributed to discussions and provided input on the manuscript.

Competing interests

The authors declare no competing interests.

Additional information

Extended data is available for this paper at https://doi.org/10.1038/s41561-026-01922-5.

Supplementary information The online version contains supplementary material available at https://doi.org/10.1038/s41561-026-01922-5.

Correspondence and requests for materials should be addressed to Jingyi Li or Xinlei Ge.

Peer review information *Nature Geoscience* thanks the anonymous reviewer(s) for their contribution to the peer review of this work.

Primary Handling Editor: Carolina Ortiz Guerrero and Aliénor Lavergne, in collaboration with the *Nature Geoscience* team.

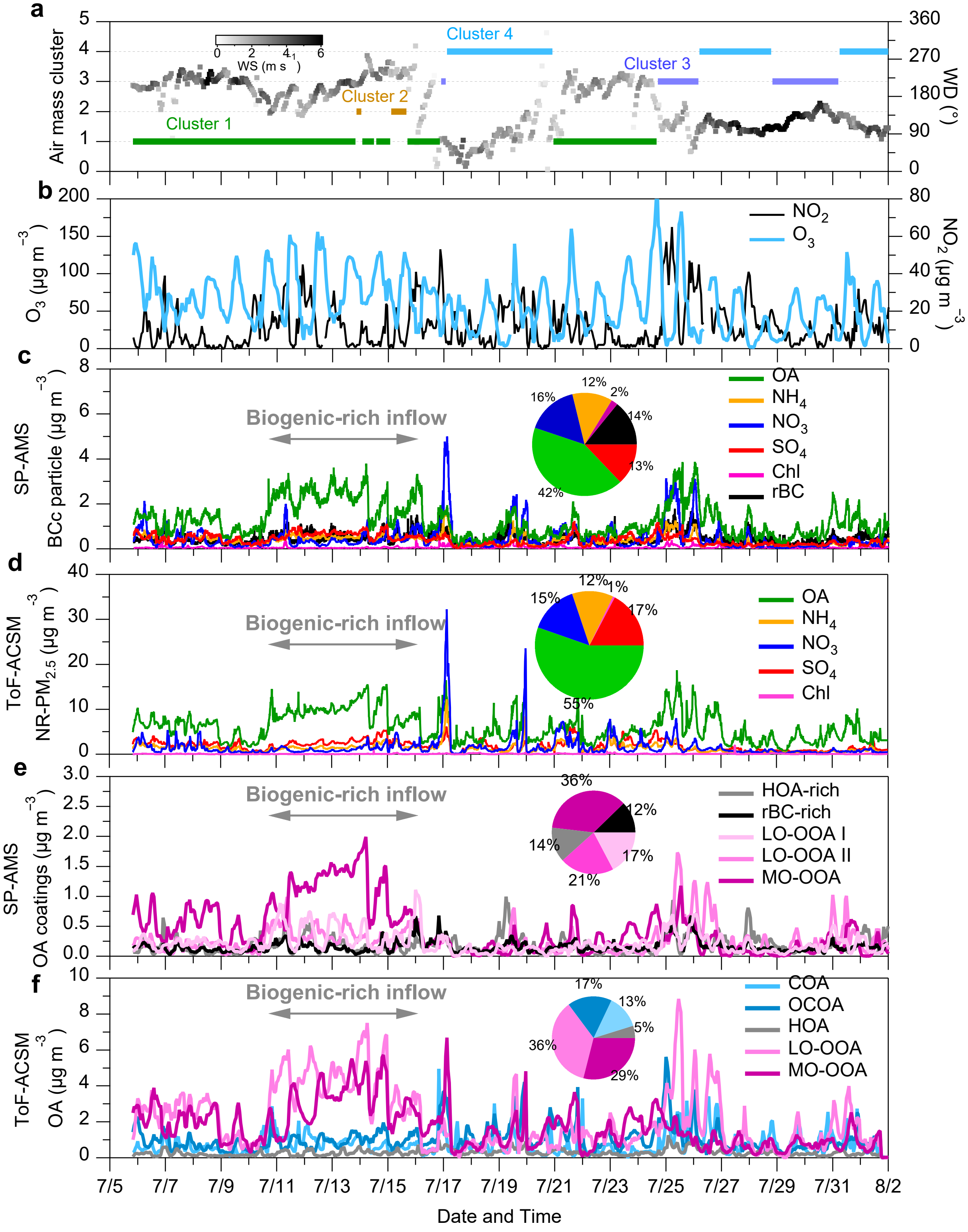

Extended Data Fig. 1 | Time series of chemical composition of BC-containing particles and bulk aerosol in NR-PM$_{2.5}$, trace gases, and meteorological parameters. **a.** Wind speed, wind direction, and clustered 2-day air mass backward trajectories (see Supplementary Fig. 1 for clustering geographic distribution). **b.** Time series of surface O_3 and NO_2 concentrations. **c.** Chemical composition of coatings on BC-containing particles. **d.** Bulk chemical composition of NR-PM$_{2.5}$. **e.** Source apportionment of organic aerosol coatings of BC-containing particles. **f.** Source apportionment of bulk organic aerosol in NR-PM$_{2.5}$.

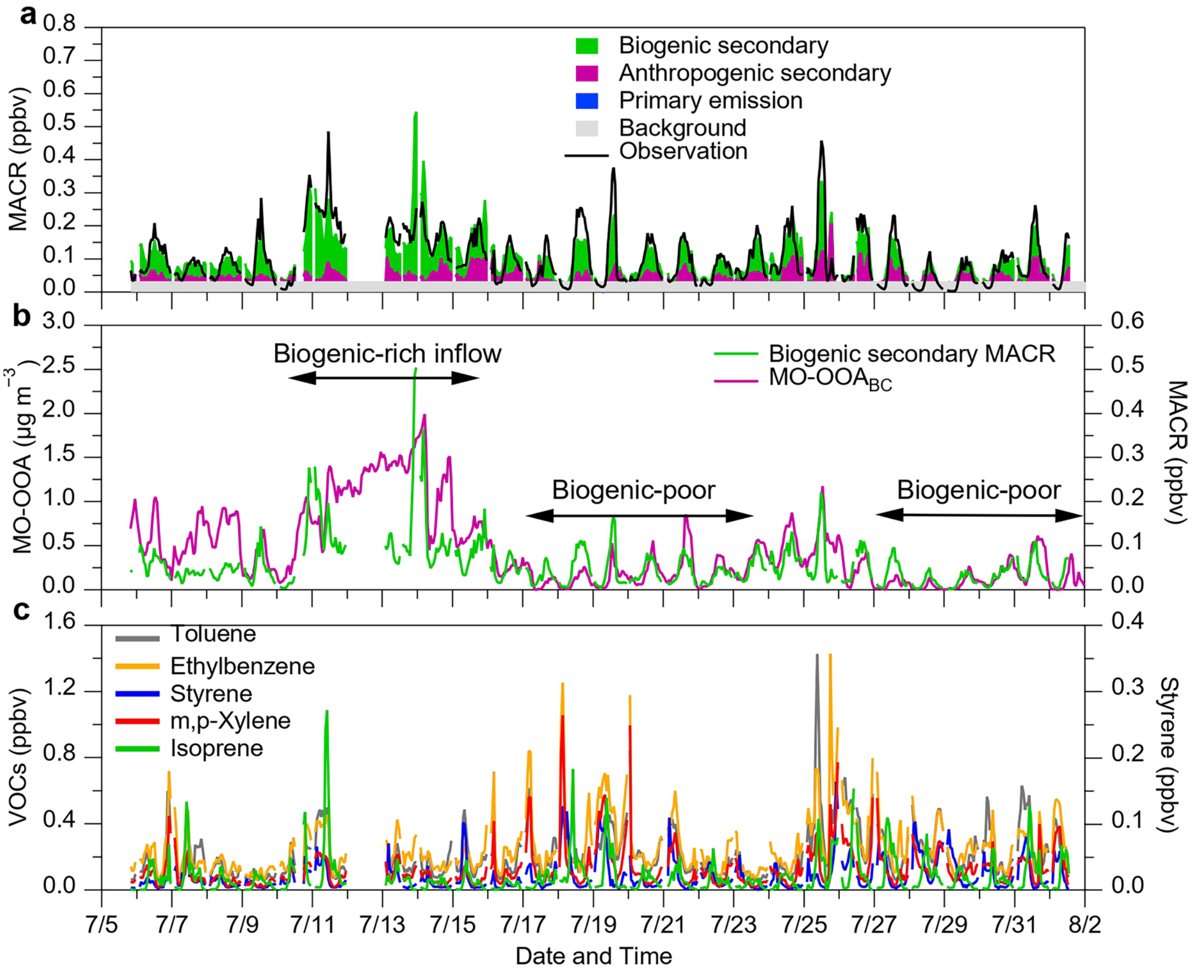

Extended Data Fig. 2 | Source apportionment of methacrolein (MACR) and temporal evolution of MO-OOA$_{BC}$ and VOCs. a. Time series of MACR contributions from different sources, including biogenic secondary, anthropogenic secondary, and background levels. **b**. Time series of MO-OOA$_{BC}$ and biogenic MACR. **c**. Time series of major anthropogenic and biogenic VOCs.

https://doi.org/10.1038/s41561-026-01922-5

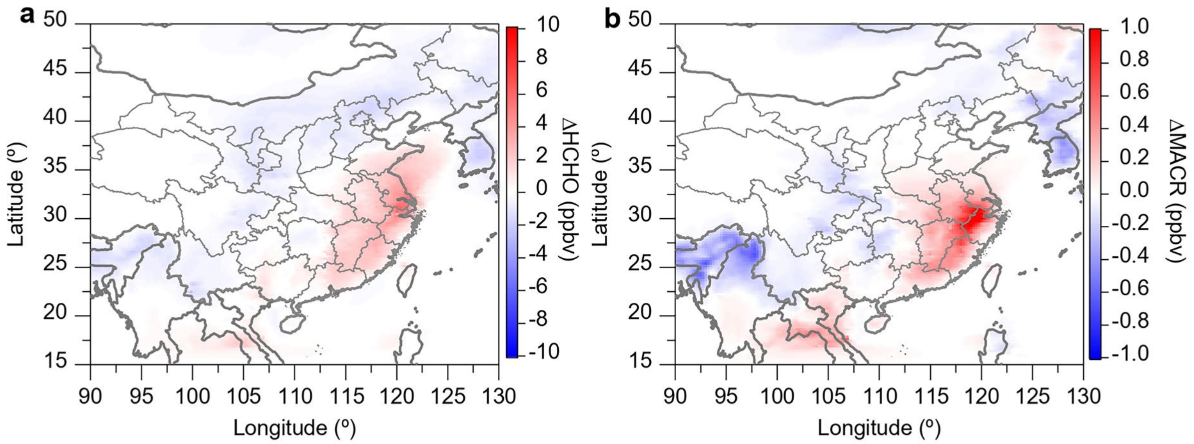

Extended Data Fig. 3 | Biogenic-enhanced oxygenated productions. a. and **b**. Simulated differences in surface HCHO and MACR concentrations between biogenic-rich and biogenic-poor periods.

https://doi.org/10.1038/s41561-026-01922-5

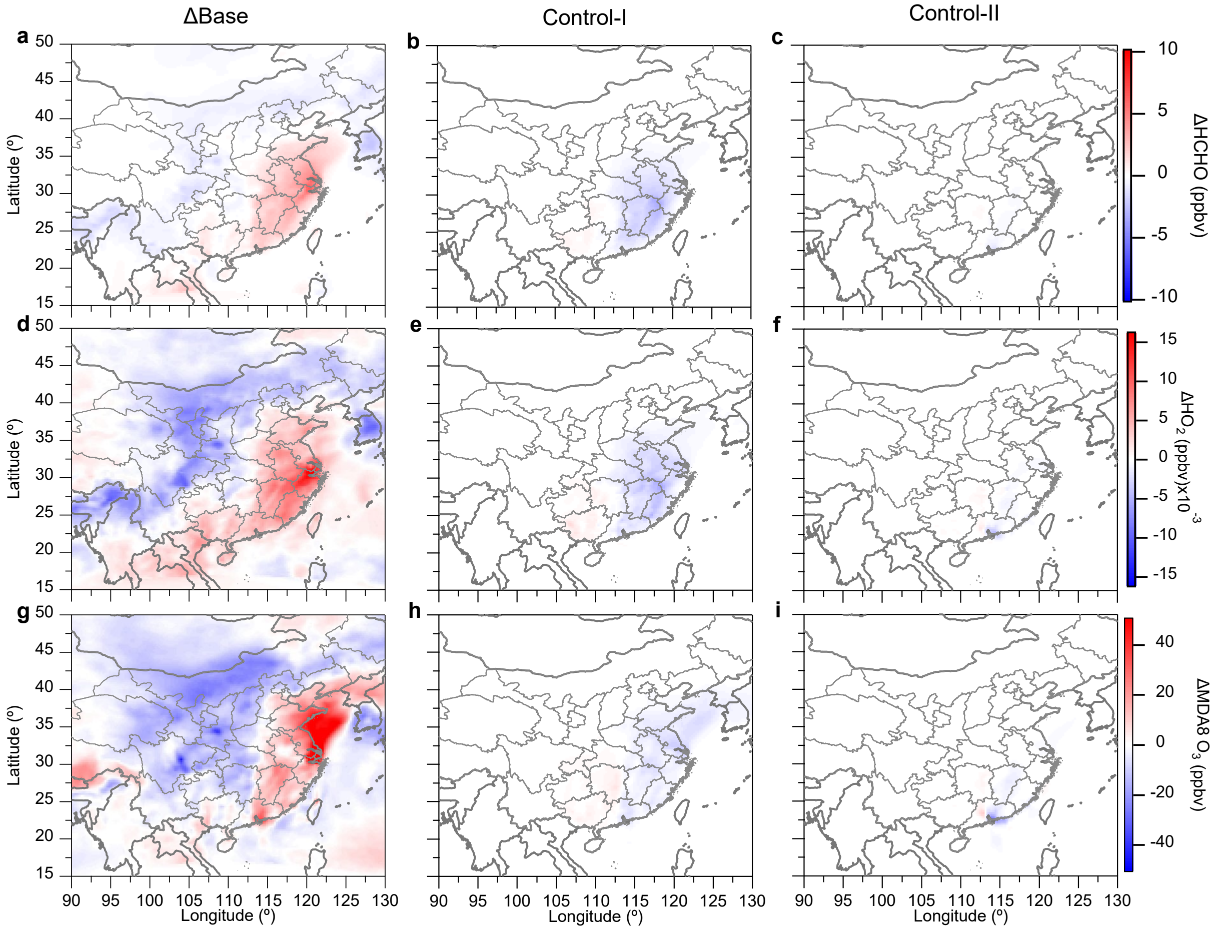

Extended Data Fig. 4 | Sensitivity of atmospheric oxidants to emissions. The first column (ΔBase, **a, d, g**) shows differences of HCHO, HO_2 radical, and MDA8 O_3 concentrations between biogenic-rich and biogenic-poor in the base case, which are defined as delta. The second (Control-I, **b, e, h**) and third column (Control-II, **c, f, i**) show the differences in delta between sensitivity cases and the base case. For the two sensitivity cases, emissions of biogenic VOCs (Contro-I) and anthropogenic VOCs (Control-II) in the SEC region are set to zero.

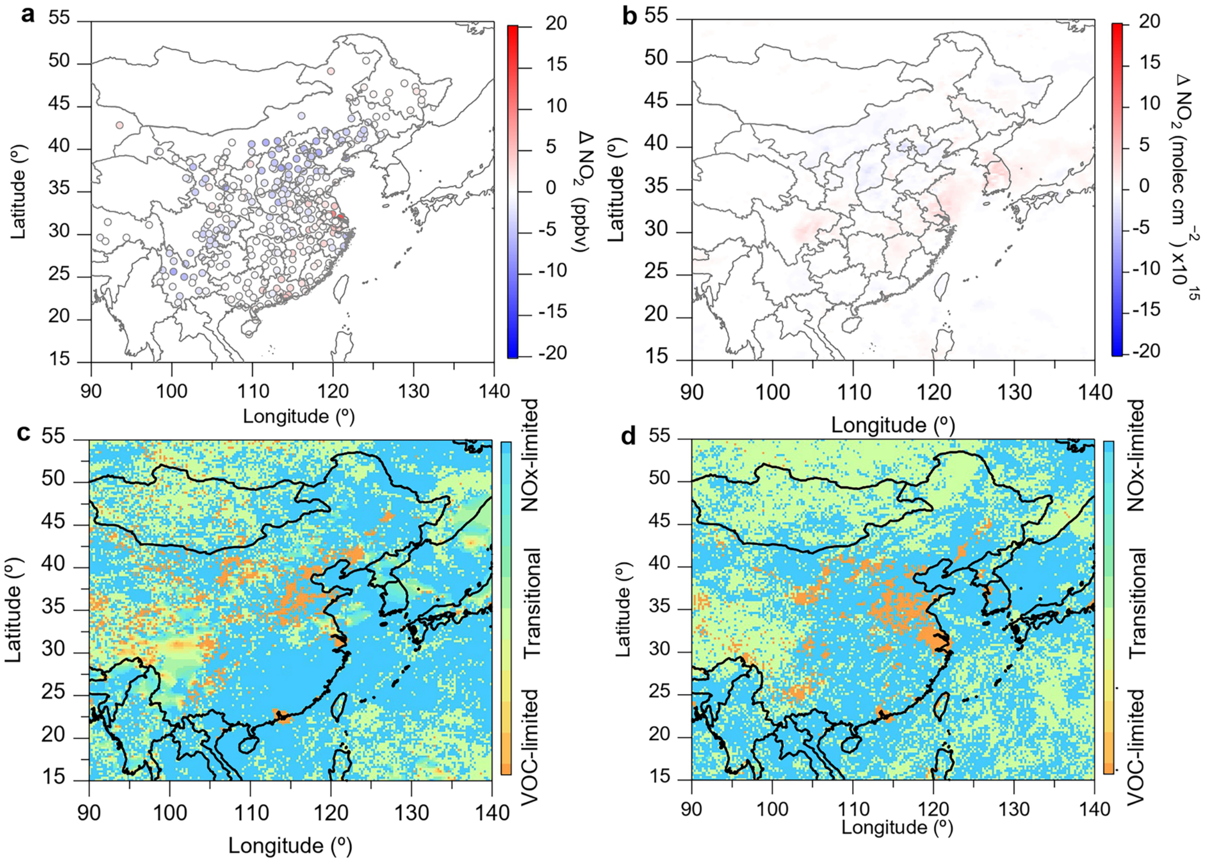

Extended Data Fig. 5 | Distribution of observed NO$_2$ concentrations and ozone production regimes. a. Surface-observed NO$_2$ concentration differences between biogenic-rich and biogenic-poor periods, respectively. **b.** Same as a, but for tropospheric NO$_2$ column densities retrieved from satellite observations. **c.** and **d.** Ozone production regime classifications – VOC-limited, NO$_x$-limited, and transitional – identified based on the satellite-derived HCHO/NO$_2$ column ratio method during biogenic-rich (**c**) and biogenic-poor (**d**) conditions, respectively.

https://doi.org/10.1038/s41561-026-01922-5

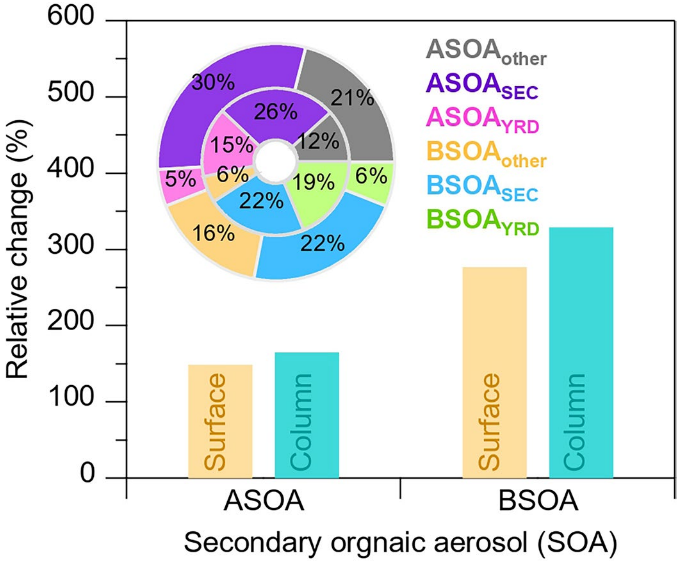

Extended Data Fig. 6 | Source apportionment of secondary organic aerosols. Relative changes in anthropogenic SOA (ASOA) and biogenic SOA (BSOA) for both surface and column concentrations between biogenic-rich and biogenic-poor periods (bar plots). Pie charts show source apportionment of ASOA and BSOA during biogenic-rich periods in the YRD; inner and outer rings represent contributions to surface and column SOA, respectively.

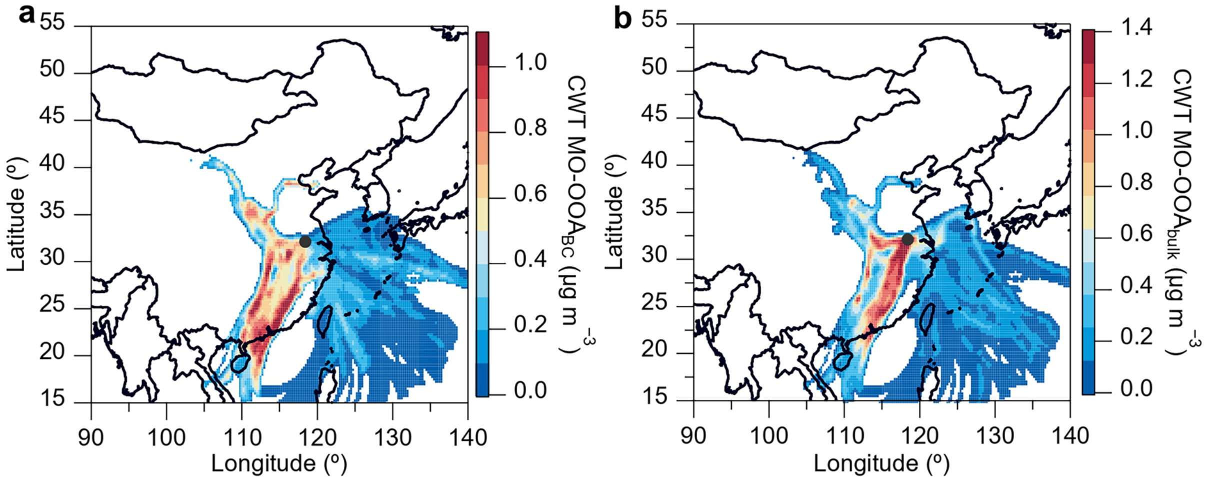

Extended Data Fig. 7 | Geographical origins of secondary organic aerosols. a and **b**. Two-day backward dispersion maps for air masses arriving at the Nanjing sampling site (black solid circle), based on the CWT method. Shown are CWT-derived source regions associated with elevated mass concentrations of (**a**) MO-OOA$_{BC}$ and (**b**) MO-OOA$_{bulk}$.